J. Fluid Mech. (2011), *vol.* 667, *pp.* 1–37.
doi:10.1017/S0022112010003988

Near-wall turbulence statistics and flow structures over three-dimensional roughness in a turbulent channel flow

JIARONG HONG[1], JOSEPH KATZ[1]† AND MICHAEL P. SCHULTZ[2]

[1]Department of Mechanical Engineering, The Johns Hopkins University, Baltimore, MD 21218, USA

[2]Department of Naval Architecture and Ocean Engineering, United States Naval Academy, Annapolis, MD 21402, USA

(Received 16 April 2010; revised 23 July 2010; accepted 24 July 2010)

Utilizing an optically index-matched facility and high-resolution particle image velocimetry measurements, this paper examines flow structure and turbulence in a rough-wall channel flow for Re_τ in the 3520–5360 range. The scales of pyramidal roughness elements satisfy the 'well-characterized' flow conditions, with $h/k \approx 50$ and $k^+ = 60 \sim 100$, where h is half height of the channel and k is the roughness height. The near-wall turbulence measurements are sensitive to spatial resolution, and vary with Reynolds number. Spatial variations in the mean flow, Reynolds stresses, as well as the turbulent kinetic energy (TKE) production and dissipation rates are confined to $y < 2k$. All the Reynolds stress components have local maxima at slightly higher elevations, but the streamwise-normal component increases rapidly at $y < k$, peaking at the top of the pyramids. The TKE production and dissipation rates along with turbulence transport also peak near the wall. The spatial energy and shear spectra show an increasing contribution of large-scale motions and a diminishing role of small motions with increasing distance from the wall. As the spectra steepen at low wavenumbers, they flatten and develop bumps in wavenumbers corresponding to $k - 3k$, which fall in the dissipation range. Instantaneous realizations show that roughness-scale eddies are generated near the wall, and lifted up rapidly by large-scale structures that populate the outer layer. A linear stochastic estimation-based analysis shows that the latter share common features with hairpin packets. This process floods the outer layer with roughness-scale eddies, in addition to those generated by the energy-cascading process. Consequently, although the imprints of roughness diminish in the outer-layer Reynolds stresses, consistent with the wall similarity hypothesis, the small-scale turbulence contains a clear roughness signature across the entire channel.

Key words: boundary layers, boundary layer structure, turbulent boundary layers

1. Introduction

In a comprehensive review, Raupach, Antonia & Rajagopalan (1991) extend the Reynolds number similarity hypothesis of Townsend (1976) to flow over rough walls. In their wall similarity hypothesis, they state that outside of the 'roughness sublayer', turbulent motions in a boundary layer at high Reynolds numbers are independent

† Email address for correspondence: katz@jhu.edu

of the wall roughness and viscosity. This roughness sublayer, extending from the wall up to 2–5 roughness length scales (typically k), is the region where the flow is dynamically influenced by length scales associated with the roughness elements. Since then, numerous studies have investigated the validity and applicability of this hypothesis, too many to summarize in a single paper. Strong support has been provided recently for zero-pressure-gradient (ZPG) boundary layer flows over three-dimensional roughness by e.g. Schultz & Flack (2003) and Flack, Schultz & Shapiro (2005). Conversely, some other ZPG boundary layer studies (e.g. Krogstad, Antonia & Browne 1992; Krogstad & Antonia 1999; Tachie, Bergstrom & Balachandar 2000, 2003; Keirsbulck *et al.* 2002), have observed significant changes to the Reynolds stresses that extend well into the outer layer for flows over woven mesh and transverse bar roughness. By examining data presented in previous papers, Jiménez (2004) points out that most rough-wall studies have had a low value of either scale separation δ/k (δ being the boundary layer thickness) or the equivalent sand roughness Reynolds number, $k_s^+ = U_\tau k_s/\nu$ (where U_τ is the friction velocity and k_s is the equivalent sand roughness height). In the former case, the flow can be better described as turbulence over obstacles, while in the latter case, flows are located in the transitionally rough regime. To obtain a 'well-characterized' rough-wall turbulent boundary layer for examining Townsend's hypothesis, both k^+ and δ/k must exceed threshold values (typically $k^+ > 50$–10 and $\delta/k > 40$), and their product, i.e. δ^+, should be at least 4000. Following this guidance, recent experiments (e.g. Shockling, Allen & Smits 2006; Wu & Christensen 2007; Schultz & Flack 2007; Volino, Schultz & Flack 2009) have shown that the wall similarity hypothesis holds in ZPG turbulent boundary layers over three-dimensional roughness that satisfy the well-characterized condition. Krogstad *et al.* (2005) and Bakken *et al.* (2005) show that the same conclusions apply to turbulent channel flows over two-dimensional and three-dimensional roughness on both the bottom and top walls, even when the flow conditions do not strictly attain Jiménez's threshold for well-characterized flow. The only exception has been reported for a ZPG boundary layer with a two-dimensional roughness (e.g. Djenidi *et al.* 2008). When the flow satisfies the wall similarity hypothesis, the impact of roughness on the outer layer can be accounted for as a mean momentum deficit whose magnitude depends on the roughness geometry. All other effects associated with the surface condition are confined to the roughness sublayer. The motivation for studying the roughness sublayer is not only to associate the local turbulence statistics with geometric parameters of the rough surface but also to elucidate the fundamental processes involved, and understand how they affect the influence zone of roughness. Answering these questions is essential for the development of appropriate modelling tools.

However, due to characteristics of near-wall flow phenomena, the current flow measurement techniques encounter unavoidable challenges. The accuracy of traditional single-point measurement techniques, such as hot-wire probes, is adversely affected by the high-intensity turbulence as well as low mean velocity near and within the roughness (Raupach *et al.* 1991). Nonetheless, until recently, most of our experimental data on the rough-wall boundary layer have been obtained using hot wires (e.g. Perry, Lim & Henbest 1987; Perry & Li 1990; Krogstad *et al.* 1992). Optical techniques such as laser Doppler velocimetry (LDV) and particle image velocimetry (PIV) are susceptible to interfacial reflection at the solid surface, which leads to signal deterioration in the near-wall measurements. In the few cases that have focused on the roughness sublayer, the experimental set-ups are located in the low δ/k regime (e.g. Grass 1971; Dancey *et al.* 2000). Owing to the rapid advances on

computation speed, direct numerical simulations (DNS) have been applied extensively to study turbulence over smooth walls at increasingly higher Reynolds numbers, e.g. $Re_\tau = 180$ (Kim, Moin & Moser 1987), $Re_\tau = 590$ (Moser, Kim & Mansour 1999) and $Re_\tau = 2000$ (Hoyas & Jiménez 2008). However, adapting this tool for rough-wall turbulence requires much denser computational grids to resolve the three-dimensional roughness topography and neighbouring flow structures. Consequently, the DNS of rough-wall turbulence has been mostly implemented for two-dimensional roughness. The corresponding Reynolds numbers are relatively low compared with experiments even for the latest simulations, e.g. at $Re_\theta = 1400$ in a boundary layer (Lee & Sung 2007) and at $Re_\tau = 730$–1064 in channel flows (Burattini *et al.* 2008). For the DNS of the flow above three-dimensional roughness, the achievable Reynolds number is even lower, e.g. $Re_\tau = 400$ (Bhaganagar, Kim & Coleman 2004). In these cases, the flows are either located in the transitionally rough regime (low k_s^+) or close to the flow over obstacles (low δ/k). Except for the study by Bhaganagar *et al.* (2004), the distributions of roughness elements are also sparse, with the distance between them exceeding $4k$. Nevertheless, some recent two-dimensional, sparse roughness studies have provided valuable information on flow structures and turbulence statistics in the roughness sublayer. For instance, in the DNS of a turbulent channel flow over two-dimensional ribs by Ikeda & Durbin (2007), they observed that disruption of the three-dimensional vortical streak in the roughness sublayer is responsible for high energy production just above the roughness. With a similar rough surface configuration in a ZPG boundary layer, Lee & Sung (2007) report a significant effect of roughness on the redistribution of TKE near the wall. The experimental results of Djenidi *et al.* (2008) reveal that roughness-scale spanwise vortices originating at the trailing edge of the roughness are convected downstream and strongly interact with the overlying turbulent flow. In summary, to our knowledge, none of the experimental or computational studies to-date have resolved the turbulence in the roughness sublayer of a well-characterized boundary layer or channel flow over a dense three-dimensional rough wall.

Consequently, the objective of our project is to conduct detailed near-wall flow measurements under the constraint of well-characterized conditions, and then use the data for elucidating the dominant contributors to turbulence there. By utilizing an optically refractive index-matched test facility and high resolution PIV, we are able to overcome the aforementioned obstacles and conduct measurements that resolve the flow in the roughness sublayer. The present paper begins with a brief description of the experimental set-up, measurement techniques and data process procedures in § 2. In § 3.1, data on the spatially averaged mean flow and Reynolds stresses are provided, followed by a discussion of the spatial resolution and Reynolds number effect on Reynolds stress measurements. Turbulence statistics in the roughness sublayer are discussed in § 3.2, including spatial variations in Reynolds stresses and other terms affecting the TKE budget. Finally, in § 3.3, we apply spectral analysis, swirling-strength-based linear stochastic estimation (LSE) along with instantaneous observations to study the flow structures from near the wall to the lower portion of the outer layer.

2. Experimental set-up and methodology

2.1. *Facility and measurement*

The experiment is performed in the bypass channel of our waterjet pump test facility, as illustrated in figure 1. The entire facility is filled with 62 % by weight solution of sodium iodide (NaI) in water that has the same optical refractive index (1.492)

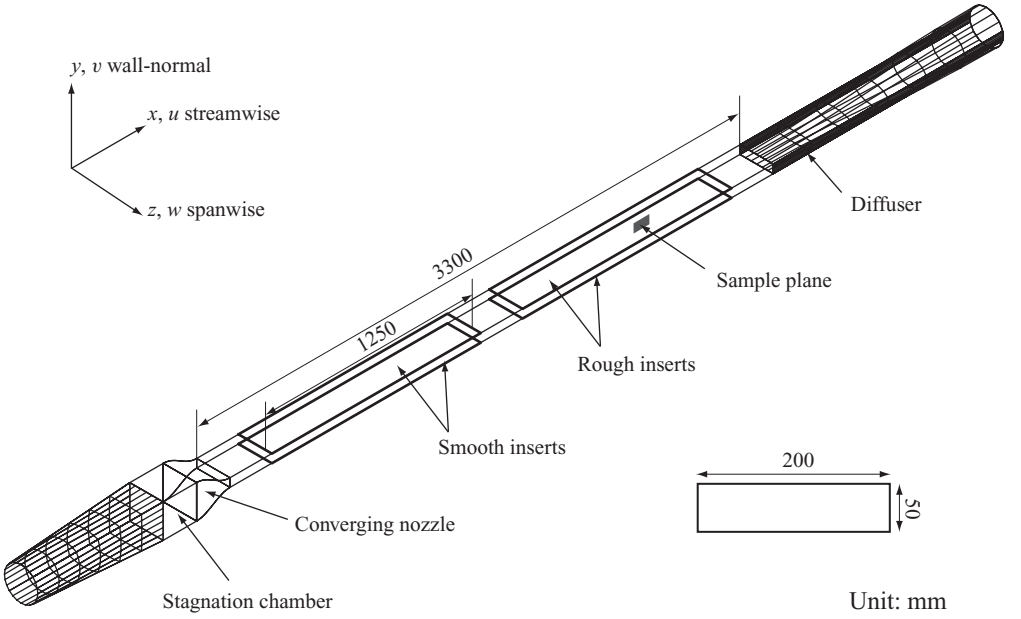

FIGURE 1. Bypass channel in the optically index-matched test facility.

as acrylic. The specific gravity of this fluid is 1.8, and its kinematic viscosity (ν) is $1.1 \times 10^{-6}\,\mathrm{m^2\,s^{-1}}$ at ambient temperature, making it a suitable substitute for water. Using this technique, previous experiments (e.g. Soranna *et al.* 2006) have successfully resolved complex flow fields and turbulence in the vicinity of acrylic blades of turbomachines. The bypass channel consists of an independent settling chamber, a converging nozzle, a test section and diffuser. The test section is a 3.3 m long and $20 \times 5\,\mathrm{cm^2}$ rectangular cross-section duct, made entirely of acrylic material, which facilitates optical access to any internal site from various viewing angles. Note that the 4:1 aspect ratio of the duct is not sufficient to claim that the present channel flow conditions are two-dimensional. For example, based on information provided by Leutheusser (1963), Dean (1978) and Monty (2005), the ratio of the wall shear stress to $h\partial p/\partial x$ ($\partial p/\partial x$ is the mean pressure gradient) in a 4:1 aspect ratio channel/duct is only about 0.93 as opposed to 1.0 for a two-dimensional flow. For low aspect ratio duct flows, i.e. 1:1 and 2:1, it has been shown that roughness enhances the secondary flows, but their characteristic magnitude remains below 2–3 % of the streamwise centreline velocity (Fujita, Yokosawa & Hirota 1989; Yokosawa *et al.* 1989). Thus, although we use the term channel throughout this paper, note that the present flow is not fully two-dimensional.

Two pairs of 1.25 m long removable acrylic inserts are mounted in the upstream and downstream halves of the test section. Each pair has a symmetric top and bottom plate that face each other. This study is performed with a pair of smooth inserts upstream and a pair of rough inserts downstream. According to Antonia & Luxton (1971), to achieve a self-similar rough-wall boundary layer, one must have a sufficient streamwise fetch with roughness of approximately 15δ–20δ. Although this criterion may not apply directly to a channel flow, it has been used as guidance and subsequently verified based on the present data. As illustrated in figure 2(a), our measurements are conducted near $35h$ from the leading edge of the rough insert. In our region of interest, i.e. between $34h$ and $36h$, the average streamwise deviation in the

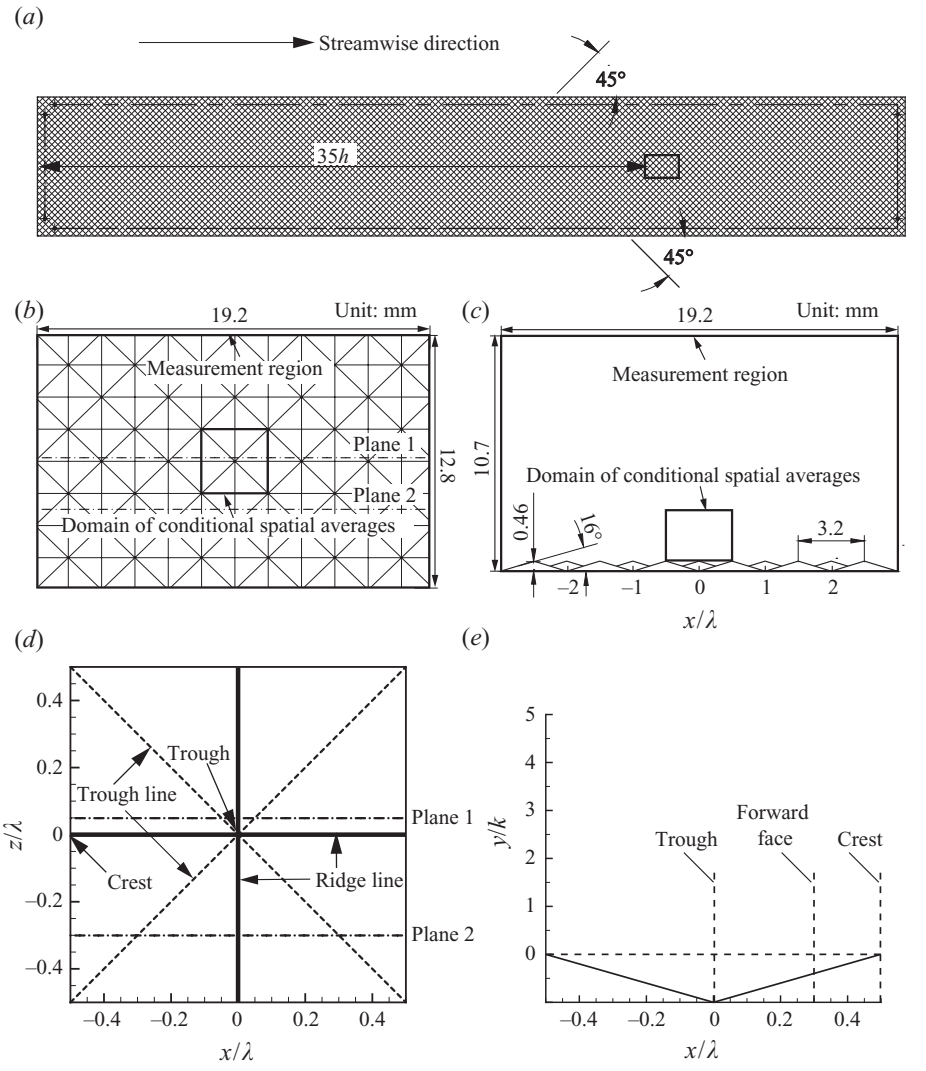

FIGURE 2. (*a*) The rough insert plate showing the measurement region marked by a rectangle. (*b*) An *x*–*z* projection of the sample area showing the centreline of the two investigated *x*–*y* planes and the domain used for presenting conditional spatial averages. (*c*) The dimensions of the wall roughness, *x*–*y* plane 1 and domain of the conditional spatial averages. (*d*) An *x*–*z* plane and (*e*) *x*–*y* plane 1 of the conditional spatial averages.

mean streamwise velocity magnitude is $\sim 0.4\,\%$, and the deviations in the Reynolds stress components are 0.5 % for $\langle u'u' \rangle$, 1.1 % for $-\langle u'v' \rangle$ and 1.6 % for $\langle v'v' \rangle$. These values are lower than the corresponding uncertainty levels (details follow). We use these results along with the streamwise location of measurements ($35h$) as justification for assuming that the flow has achieved self-similarity. The rough surface is composed of closely packed pyramidal elements, which are illustrated in figures 2(*a*) and 2(*b*). This type of roughness has well-defined length scales, and its height k and wavelength λ make it sufficiently simple for performing spatial sampling of data while retaining the three-dimensional nature of the roughness. The individual pyramid in our study is 0.46 mm in height and has a slope angle of 16° (figure 2*c*), which falls in the middle

U_c (m s^{-1})	Re_h	k (mm)	k_s^+	$U_{\tau-log}$(m s^{-1})	$U_{\tau-uv}$(m s^{-1})	Wall unit (μm)	Re_τ
2.75	62 500	0.46	95	0.159	0.155	7.1/7.3	3520
3.24	73 640		113	N/A	0.181	6.1	4110
3.75	85 230		130	N/A	0.206	5.3	4680
4.26	96 820		147	N/A	0.236	4.7	5360

TABLE 1. Experimental flow conditions.

of a series of pyramidal shapes tested by Schultz & Flack (2009). For the selected roughness, both their data and the present mean velocity profile (figure 5*a*) have shown that $k_s \sim 1.5k$. As a result, according to the measured friction velocity shown in table 1, our rough-wall flow yields $\delta/k > 50$ (using $\delta = h$) and $k_s^+ > 80$, satisfying the well-characterized condition proposed by Jiménez (2004).

To obtain a full picture of the flows in the roughness sublayer, PIV measurements are conducted both at the x–y and x–z planes, where the (x, y, z) conventions are defined in figure 1. Measurements in the x–y plane are carried out at two spanwise locations, as illustrated in figure 2(*b*), in close proximity to the centreline of the channel. Accordingly, the x–z plane measurement (figure 2*b*) covers the same spanwise locations, at multiple elevations above the wall within the roughness sublayer. The laser sheet is generated by a 120 mJ/pulse Nd:YAG laser, and has a thickness of ~ 0.5 mm, i.e. 15 % of λ and about equal to k. The fluid is seeded with 2 μm silver-coated glass particles, with specific gravity of 3.1. The illuminated particle images are recorded by a 4864×3248 pixel interline transfer CCD camera. The acquisition rate of image pairs is 1 Hz with an in-pair pulse delay of 50 μs, making the samples statistically independent. The resulting typical particle image diameter is 2–3 pixels. Images are enhanced using procedures described in Roth, Mascenik & Katz (1999), with velocity vectors obtained using multi-path cross-correlations in LaVision DaVis® software. The final interrogation window size is 32×32 pixels, and vectors are calculated with 50 % overlap. Based on the characteristic displacement of 10–35 pixels between exposures and an estimated 0.1–0.2 pixel uncertainty in the displacement measurement using cross-correlation, the uncertainty in the instantaneous velocity is 0.5–2 %. Since the particle diameter is more than 2 pixels, the so-called peak locking bias error is minimal and of the same magnitude as the random uncertainty (Westerweel 1997; Christensen 2004). To evaluate the uncertainty in ensemble-averaged statistics, we have performed a bootstrap analysis by randomly selecting subsamples of 4000 data points (out of the 5000 available) and obtaining the distribution of measured statistics. Using twice the standard deviation as a criterion for uncertainty, i.e. a confidence level of 95 %, one can obtain the characteristic uncertainties for most turbulence statistics in this paper. Sample values are 0.6 % for the mean velocity, 3.8 % for $\langle u'u' \rangle$, 6.8 % for $-\langle u'v' \rangle$, 5.1 % for $\langle v'v' \rangle$, 12 % for triple correlation values (for one standard deviation), and 5.6 % for dissipation rates estimated based on local velocity gradients. However, both the Reynolds stresses and dissipation rates are also affected by the finite resolution of PIV measurements, as discussed in detail in § 3.1 and 3.2.2, respectively.

Data in the x–y planes have been obtained at two different resolutions. Low resolution measurements have vector spacing of 280 μm and cover the entire half-channel. High resolution data have vector spacing of 63 μm, corresponding to 9 wall units and $0.138k$, provide 36 rows of vectors within $5k$ and focus on examining

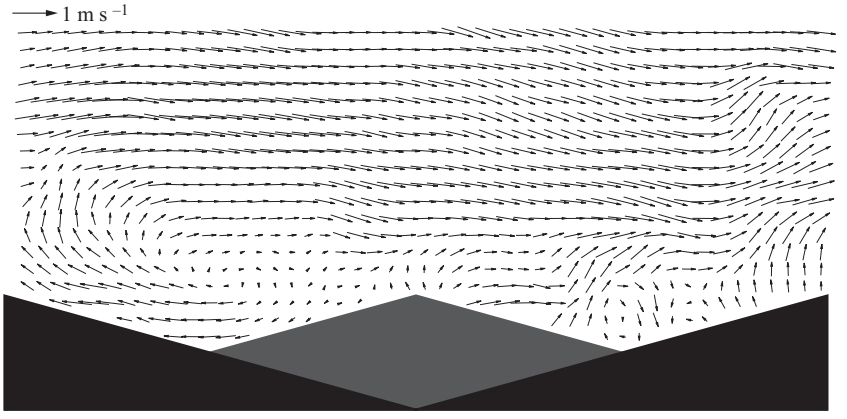

FIGURE 3. A $1\lambda \times 2k$ sample of the instantaneous near-wall flow field at x–y plane 1 and $Re_\tau = 3520$, showing the velocity distribution after subtracting $0.35U_c$ from each vector.

turbulence in the roughness sublayer. Figure 3 shows a 1λ long and $2k$ wide sample part of the vector map, illustrating our spatial resolution and near-wall measurement region all the way down to the index-matched rough surface. However, in the present paper, we provide statistics for the flow starting from the top of the roughness where $y = 0$ is set (illustrated in figure 2*e*). As a result, the closest data points to the roughness are located at $y = 36\,\mu\text{m} \sim 5$ wall units. The x–z plane measurement maintains the same resolution as the x–y plane data, but due to the laser sheet thickness, it essentially provides an average over a distance $\sim k$ in the wall-normal direction. Therefore, it is only employed for examining spatial variability in the near-wall turbulent flow. Approximately 5000 image pairs are obtained at each sample plane to achieve reasonable convergence of turbulence statistics.

The flow conditions and relevant parameters for the present measurements are listed in table 1. It also includes datasets acquired at three higher centreline velocities to examine the Reynolds number effect on the stress statistics. The magnitude of Re_h is calculated using the half channel height and centreline velocity, while Re_τ is based on the friction velocity U_τ, whose value is evaluated using two approaches. The value of $U_{\tau-log}$ is determined by a logarithmic fit to the mean velocity profile in $y = 2k$ to $0.2h$. $U_{\tau-uv}$ is obtained from the slope of a linear least-square fit to the total shear stress, i.e. the sum of viscous and Reynolds shear stresses, as shown in figure 4. A linear trend for the total stress distribution is imposed by the constant pressure gradients in the fully developed channel. The curve fitting range is chosen between $y = 0.2h$ and $0.43h$, the latter being the highest elevation in the high-resolution measurement. In the total stress approach, the friction velocity can also be determined by extrapolating a linear fit to the wall and calculating the stress based on its intercept with the wall. For a rough surface, there is an uncertainty in defining the wall location. By extrapolating the line both to the crest and base of the pyramid, we obtain that the associated uncertainty in wall stress is less than 2 %, and opt to use the crest value (at $y = 0$). It should be pointed out there is a slight difference between the friction velocities obtained from the slope and the intercept, and the difference diminishes as the Reynolds number increases. In the current measurement, the differences are 2 %, 1.1 %, 0.4 % and 0.3 % from the lowest to the highest Reynolds number, respectively. Generally, $U_{\tau-log}$ is employed for analysis of mean velocity distributions, while $U_{\tau-uv}$ is used for scaling Reynolds stresses (e.g. Bigillon, Niño & Garcia 2006). In table 1,

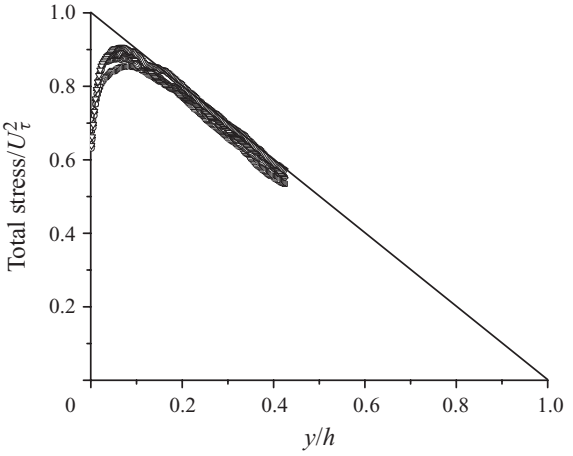

FIGURE 4. Distributions of the total shear stress fitted to the analytical distribution for total stress in the fully developed channel flow with a no-slip condition at $y = 0$ (solid line). Symbols: □, $Re_\tau = 3520$; ○, $Re_\tau = 4110$; △, $Re_\tau = 4680$; ▽, $Re_\tau = 5360$.

the value of Re_τ is calculated based on $U_{\tau-uv}$. Nevertheless, $U_{\tau-log}$ and $U_{\tau-uv}$ obtained from our dataset are very close.

2.2. *Data processing*

In the present paper, ensemble averaging, denoted by angle brackets ($\langle\,\rangle$), is first applied to obtain statistical quantities (e.g. $U = \langle u \rangle$ and $\langle u'u' \rangle$, where $u' = u - U$) at every data point of the sample area. A spatial average, denoted by an overbar, always refers to averaging along the streamwise direction over a span of 4λ. A two-step averaging refers to ensemble averaging followed by spatial averaging, and is denoted by $\overline{\langle\,\rangle}$. Since our rough surface consists of uniform and closely packed pyramids, we also perform conditional spatial averaging, which refers to spatial averaging of data at points located at the same position with respect to different pyramids (denoted by $\tilde{\langle\,\rangle}$). Taking advantage of the self-similar conditions achieved in the sample area, this process condenses the x–z data to a $\lambda \times \lambda$ square region and the x–y data to a λ wide region, as illustrated in figures 2(d) and 2(e), respectively. This averaging essentially utilizes a larger dataset to achieve better statistical convergence while maintaining the spatial variability of statistics with respect to an individual pyramid. The following quantities are calculated from the data and used during the analysis:

(a) Two point correlations are calculated at different elevations. They are defined as

$$R_{u_i u_j}(x_{ref}, y_{ref}) = \frac{\langle u_i'(x_{ref}, y_{ref}) u_j'(x_{ref} + \Delta x, y_{ref} + \Delta y) \rangle}{\sqrt{\langle u_i'(x_{ref}, y_{ref})^2 \rangle} \sqrt{\langle u_j'(x_{ref} + \Delta x, y_{ref} + \Delta y)^2 \rangle}}. \tag{2.1}$$

(b) Swirling strength is an effective indicator for vortical structures in the flow field as shown by many prior studies. It is by definition the magnitude of the imaginary part of complex eigenvalues of the velocity gradient tensor $\partial u_i / \partial x_j$ (Zhou *et al.* 1999). The two-dimensional version of this parameter, λ_{2D}, has been introduced in Adrian, Meinhart & Tomkins (2000) for analysis of two-dimensional PIV data.

(c) Linear stochastic estimation is a statistical approach to estimate the conditionally averaged flow field in the vicinity of a prescribed event (Adrian & Moin 1988; Christensen & Adrian 2001). In the present paper, we estimate the

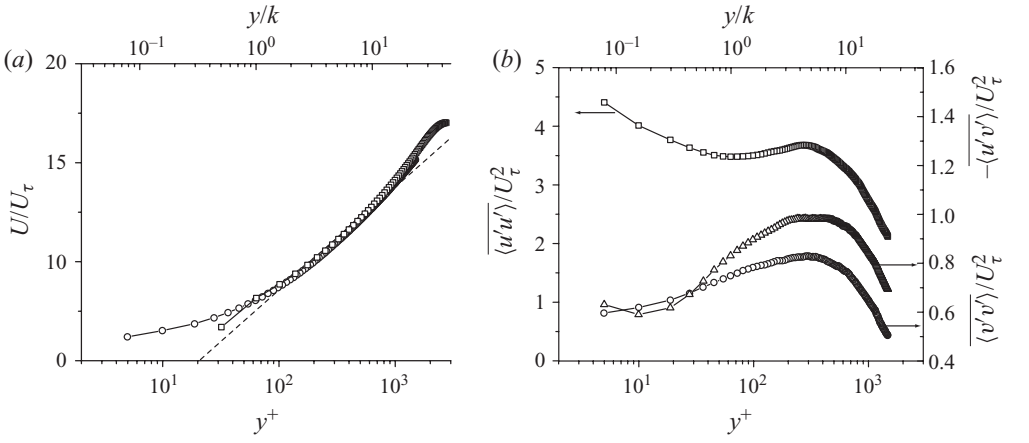

FIGURE 5. Spatially averaged quantities for x–y plane 1 and $Re_\tau = 3520$: (a) mean velocity: □, low-resolution data; ○, high-resolution data. The dashed line is a logarithmic fit to the mean velocity profile. (b) Reynolds stress components calculated using the high-resolution data: □, $\overline{\langle u'u' \rangle}$; ○, $-\overline{\langle u'v' \rangle}$; △, $\overline{\langle v'v' \rangle}$.

velocity fluctuation at $\boldsymbol{x}$ when the value of $\lambda_{2D} > 0$ at $\boldsymbol{x}_0$, i.e. $\langle u'_j(\boldsymbol{x}) \mid \lambda_{2D}(\boldsymbol{x}_0) > 0 \rangle$. The LSE of the velocity fluctuation at $\boldsymbol{x}$ is

$$\langle u'_j(\boldsymbol{x}) \mid \lambda_{2D}(\boldsymbol{x}_0) > 0 \rangle \approx \frac{\langle \lambda_{2D}(\boldsymbol{x}_0) u'_j(\boldsymbol{x}) \rangle}{\langle \lambda_{2D}(\boldsymbol{x}_0) \lambda_{2D}(\boldsymbol{x}_0) \rangle} \lambda_{2D}(\boldsymbol{x}_0). \tag{2.2}$$

This approach enables us to obtain a statistically converged estimate for the conditioned velocity field using a smaller database in comparison to that required for the direct conditional sampling.

3. Results

3.1. *Spatially averaged mean flow and Reynolds stress profiles*

Two-step-averaged mean velocity profiles are presented in figure 5(a). By combining results obtained at two different resolutions, the velocity distribution extends from the top of the roughness up to the centreline of the channel. In general, in the overlapping range, the two datasets agree very well for $y > k$. A linear region in the semi-log plot exhibits an established logarithmic layer at $2k < y < 0.2h$. The conspicuous deviation occurs below $y = k$, which includes only the lowest data point in the low resolution measurement. This discrepancy may be attributed to the relatively large uncertainty in locating the pyramid apex at this resolution. Two-step averaged Reynolds stresses of high-resolution data are presented in figure 5(b). As the figure shows, there is a local maximum of $\overline{\langle u'u' \rangle}$ at $y = 4k \sim 5k$, while $-\overline{\langle u'v' \rangle}$ and $\overline{\langle v'v' \rangle}$ have relatively broad maxima at $y = 2k \sim 6k$ and $3k \sim 8k$, respectively. At $y > 2k$, trends and magnitudes of the Reynolds stress profiles scaled with U_τ^2 agree with previously published experimental and DNS results, e.g. the compilation of the previous rough-wall measurement in Jiménez (2004), as well as computational results in Ashrafian, Andersson & Manhart (2004) and Bahaganagar *et al.* (2004). The magnitude of $\overline{\langle u'u' \rangle}$ increases again below $y = k$ as the wall is approached, peaking at the top of roughness elements. A slight increase also appears in the profile of $\overline{\langle v'v' \rangle}$ adjacent the roughness, but $-\overline{\langle u'v' \rangle}$ keeps on decreasing monotonically. It

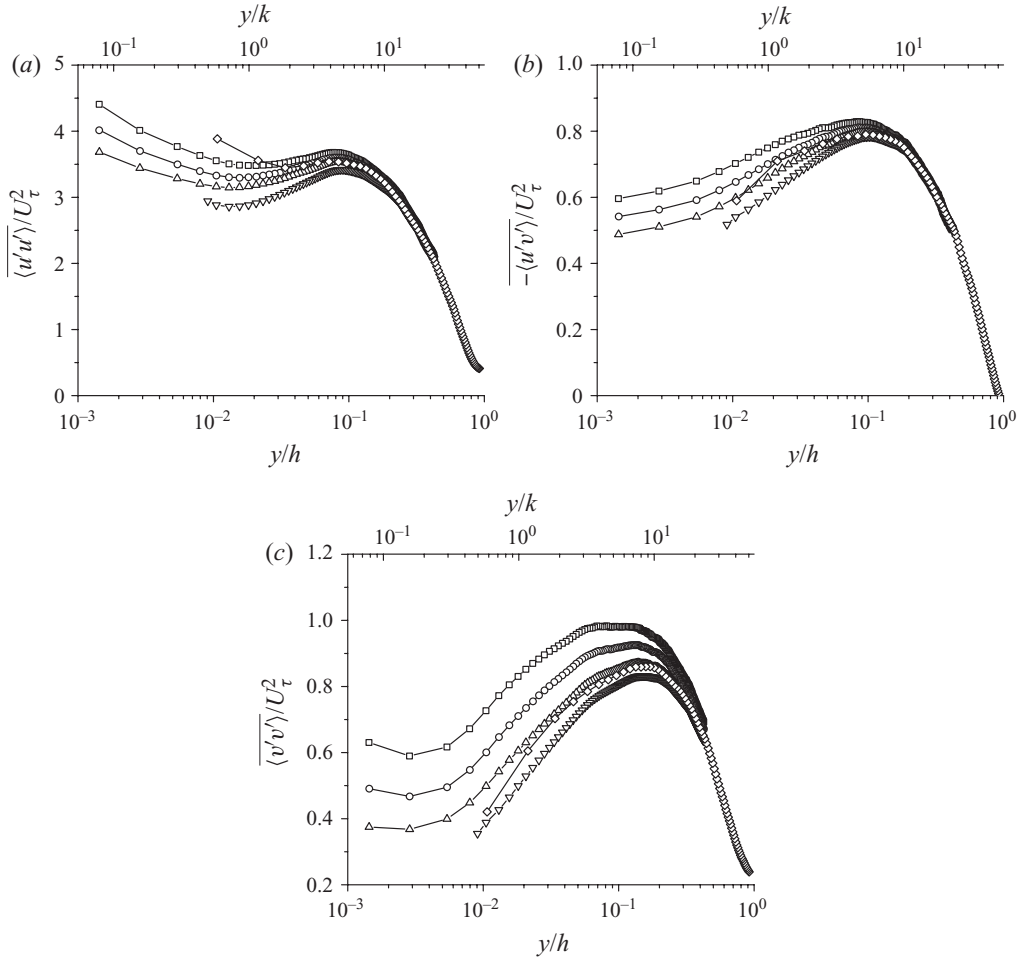

FIGURE 6. Effect of the spatial resolution on Reynolds stresses: (*a*) $\overline{\langle u'u' \rangle}$, (*b*) $-\overline{\langle u'v' \rangle}$ and (*c*) $\overline{\langle v'v' \rangle}$ at $Re_\tau = 3520$. The original high-resolution data (□) are spatially filtered by a 1×2 PIV window (○), 1×4 window (△) and 4×4 window (▽). The symbol ◇ shows low-resolution data.

is noteworthy that a similar trend of $\overline{\langle u'u' \rangle}$ is documented in Ligrani & Moffat (1986) for flows above closely packed spheres. However, they observe this near-wall upsurge only at low Reynolds numbers for a transitionally rough wall, but it vanishes with increasing k_s^+. As the authors show, their results are adversely affected by sensor resolution, and this effect increases with the Reynolds number, i.e. decreasing turbulence scales. Correspondingly, the re-appearing of the near-wall upsurge in $\overline{\langle u'u' \rangle}$ under our fully rough conditions may be well attributed to the higher spatial resolution in our study.

When approaching the wall, the contribution of small-scale motions to TKE becomes more prominent; the resolution of the turbulence measurements must be increased accordingly. To evaluate the accuracy of the present Reynolds stress measurements, we examine the effect of spatial filtering of the PIV data (prior to ensemble averaging) on the Reynolds stress statistics. This procedure essentially reduces the spatial resolution of the turbulence measurement. Figure 6 compares

profiles obtained using filters of different size and the low-resolution results with those of the original high-resolution data. In general, with increasing filter size, the magnitude of the near-wall Reynolds stresses decreases. Of the three components, the decline of $\overline{\langle v'v' \rangle}$ is the most pronounced, both in terms of magnitude and the wall-normal extent of this decay. This trend is expected since the integral scale associated with this component is of the same order as the distance from the wall, making it most affected by small-scale turbulent motions. Conversely, the streamwise components contain energy associated with much larger scale, as discussed in § 3.3. The shear stress appears to be the least sensitive to the change in the resolution near the wall. Accordingly, the correlation coefficient, i.e. $-\langle u'v' \rangle / (\sqrt{\langle u'u' \rangle}\ \sqrt{\langle v'v' \rangle})$, increases with decreasing resolution (not shown). This effect is most pronounced near the rough surface, where it reaches $\sim 20\,\%$ for the present range of filters, and diminishes in the outer layer. The effects of resolution on triple correlation terms (also not shown) are very limited for $y/k > 1$. Near the roughness, $\langle u'u'u' \rangle$ increases slightly with decreasing resolution and distance from the wall, reaching a maximum difference of $\sim 15\,\%$. Both trends are consistent with recent observations by Shah, Agelinchaab & Tachie (2008). The present trends also suggest that it is likely that even our present high resolution is still insufficient to capture all the relevant energetic small-scale turbulent motions. We will revisit this issue once higher resolution holographic data become available. The low-resolution data, whose window size is equivalent to a two-dimensional 4.4×4.4 interrogation window spacing filter, exhibit trends consistent with filtered results. They are also affected by a minor deviation in origin locations in the two different experiments, due to the increasing uncertainty in locating the pyramid apex with decreasing resolution.

Reynolds stresses measured at different Reynolds numbers are summarized in figure 7. All the stress components are scaled with corresponding U_τ^2. As is evident, all the scaled stress components increase with the Reynolds number. At $y > 0.2h$, the profiles of $\overline{\langle u'u' \rangle}$ and $\overline{\langle v'v' \rangle}$ collapse better towards the centreline of the channel. Since the curve-fitted $U_{\tau-uv}$ is dominated by the Reynolds shear stress, the $-\overline{\langle u'v' \rangle}$ profiles are matched well over the entire range. For all the stress components in the $2k < y < 10k$ range, the maxima move towards the wall with increasing Reynolds number, in agreement with previous studies (e.g. Wei & Willmarth 1989; Bakken *et al.* 2005). In the $\overline{\langle u'u' \rangle}$ and $-\overline{\langle u'v' \rangle}$ profiles, the maximum deviations occur around the stress maxima. To explain this trend, note that with increasing Reynolds number and friction velocity, the inner part of the boundary layer, where the total stress deviates from the linear fit, shrinks (figure 4). Accordingly, the maximum value of stress that fits the linear curve increases and its location moves closer to the wall with increasing Re_τ. At $y < 2k$, the Reynolds number effect on $\overline{\langle u'u' \rangle}$ and $-\overline{\langle u'v' \rangle}$ decreases relative to higher elevations but does not vanish. Conversely, profiles of $\overline{\langle v'v' \rangle}$ continue to diverge as the wall is approached. However, the difference in magnitude between $\overline{\langle v'v' \rangle}$ at the lowest and highest Reynolds number is close to that of $\overline{\langle u'u' \rangle}$. We should note that these trends are not related to the previously discussed resolution effects. Since the smallest scales of turbulence are expected to decrease with increasing Reynolds number, attenuation due to limited resolution would increase with Reynolds number. As a result, the actual near-wall Re_τ effect on $\overline{\langle v'v' \rangle}$ might be even larger than the presented trends. However, as demonstrated later, the increasing Reynolds number causes a broadband increase in turbulent energy and modifies the spectral shape for both velocity components. Consequently, attenuation by the finite resolution is not expected to play a major role in the present rough-wall channel flow.

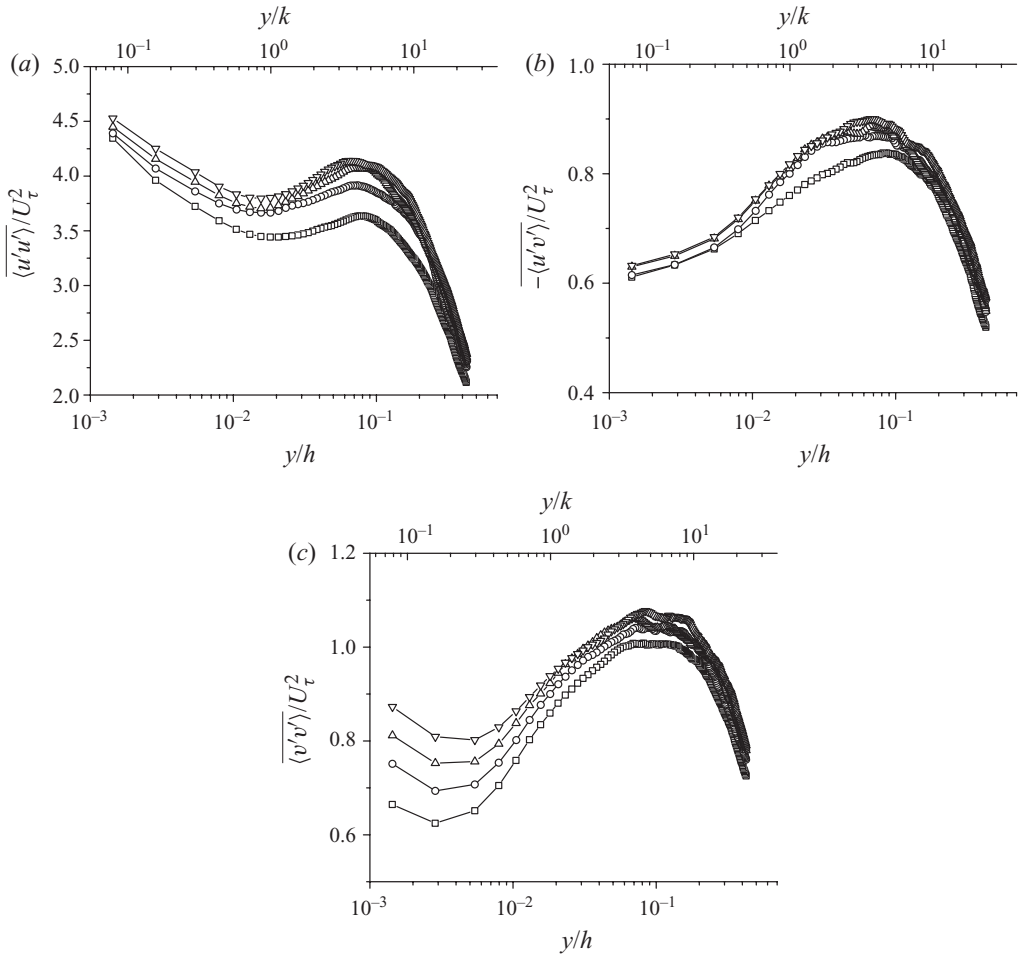

FIGURE 7. Effect of the Reynolds number on the distribution of (*a*) $\overline{\langle u'u'\rangle}$, (*b*) $-\overline{\langle u'v'\rangle}$ and (*c*) $\overline{\langle v'v'\rangle}$ in x–y plane 1. Symbols: □, $Re_\tau = 3520$; ○, $Re_\tau = 4110$; △, $Re_\tau = 4680$; ▽, $Re_\tau = 5360$.

3.2. *Spatial variation of mean flow and turbulence statistics in the roughness sublayer*

3.2.1. *Mean velocity and Reynolds stresses*

Approaching the rough surface, the flow and ensemble-averaged turbulence statistics become increasingly more susceptible to spatial variations in roughness geometry. Figure 8 is a compilation of mean flow profiles obtained from both x–y and x–z plane measurements after the conditional spatial averaging. The mean velocity profiles at $x/\lambda = 0$, 0.25, 0.5 (figure 8*a*) show no appreciable difference above $y = k$, but they diverge at lower elevations. Data for the x–z plane centred around $y = 0.4k$ show a spanwise periodic pattern with low $\widetilde{U}$ (figure 8*c*) along the streamwise ridges ($z/\lambda = 0$, the streamwise line connecting pyramid crests), and high values between them. Values of $\widetilde{U}$ are minimal around $(x/\lambda, z/\lambda) = (0.25, 0)$, i.e. above the forward-facing ridge of the pyramid. Its maxima are situated above the middle of the two spanwise ridges $(0.0, \pm 0.25)$. The maxima appearing at $x/\lambda = \pm 0.5$ are located above spanwise ridges of pyramids that are staggered by half a wavelength on either side of the target pyramid. The corresponding symmetric pattern of the spanwise velocity $\widetilde{W}$ (figure 8*d*)

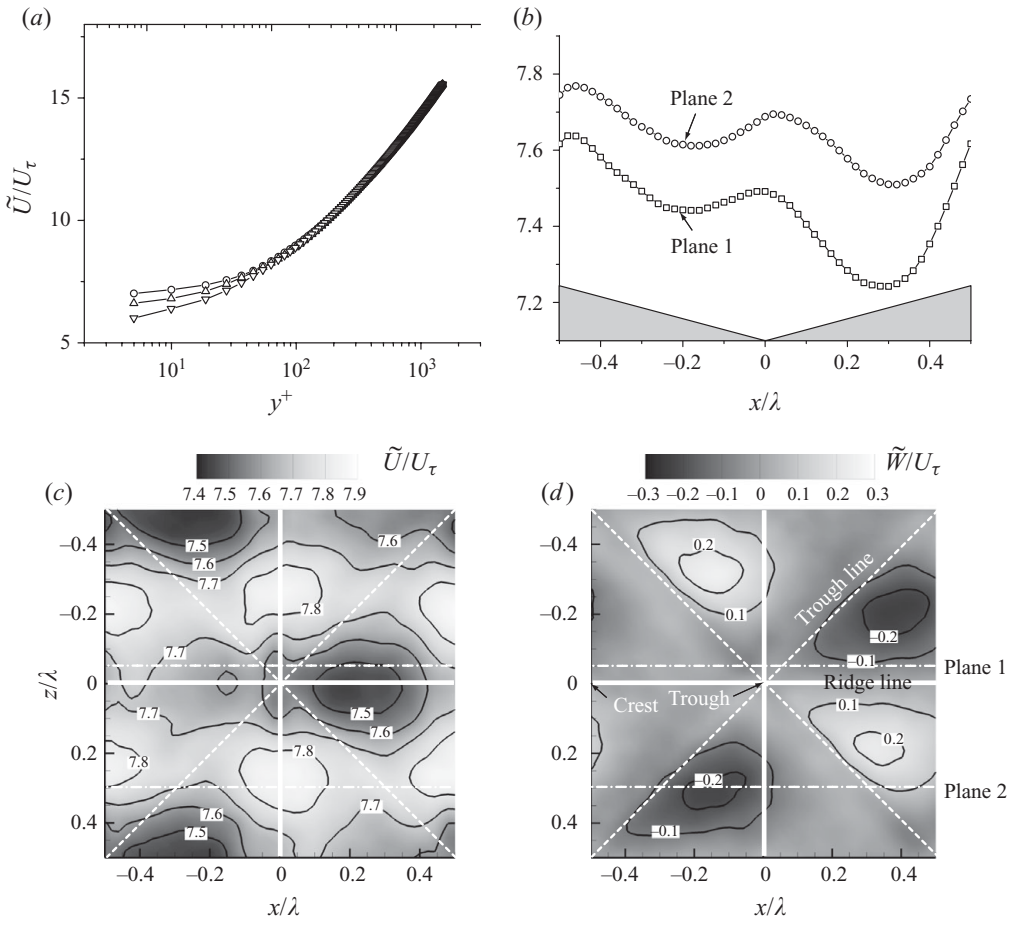

FIGURE 8. Conditionally spatially averaged mean velocity distribution at $Re_\tau = 3520$. (*a*) Streamwise velocity in x–y plane 1 and $x/\lambda = 0$ (△), 0.25 (▽) and 0.5 (○). (*b*) Streamwise velocity spatially averaged over $0 < y < 0.8k$ for x–y plane 1 (□) and 2 (○). (*c*) Streamwise and (*d*) spanwise velocity components in an x–z plane centred at $y = 0.4k$.

is also evident, with peak magnitude above the forward faces, including the target pyramid at $(0.4, \pm 0.25)$ and staggered ones on its sides. The x–y plane data averaged over $0 < y < 0.8k$ (figure 8*b*) provide a consistent picture of streamwise variations at two spanwise locations. Differences in values are attributed to the finite thickness of the laser sheet ($>k$), which results in spatial averaging in the spanwise direction.

The spatial variations in $\langle u'u' \rangle$, $-\langle u'v' \rangle$ and $\langle v'v' \rangle$ diminish above $y = 2k$, and, as a result, we use this elevation as a definition for the height of the roughness sublayer. However, all stress components become periodically non-uniform at lower elevations, as demonstrated by a sample contour of $\langle u'u' \rangle$ in figure 9(*a*). The conditional spatially averaged versions (figure 9*b*–*d*) provide more distinct patterns of these spatial variations. For $\widetilde{\langle u'u' \rangle}$ (figure 9*b*), the near-wall range contains two layers, the lower one with high values and the upper one with relatively low values. The high stress layer starts just above the crest and is initially inclined at a very shallow angle, but the inclination increases to about 15° above the forward ridge, where $\widetilde{\langle u'u' \rangle}$ is maximum. The adjacent low stress layer extends up to about $2k$ at an inclination of

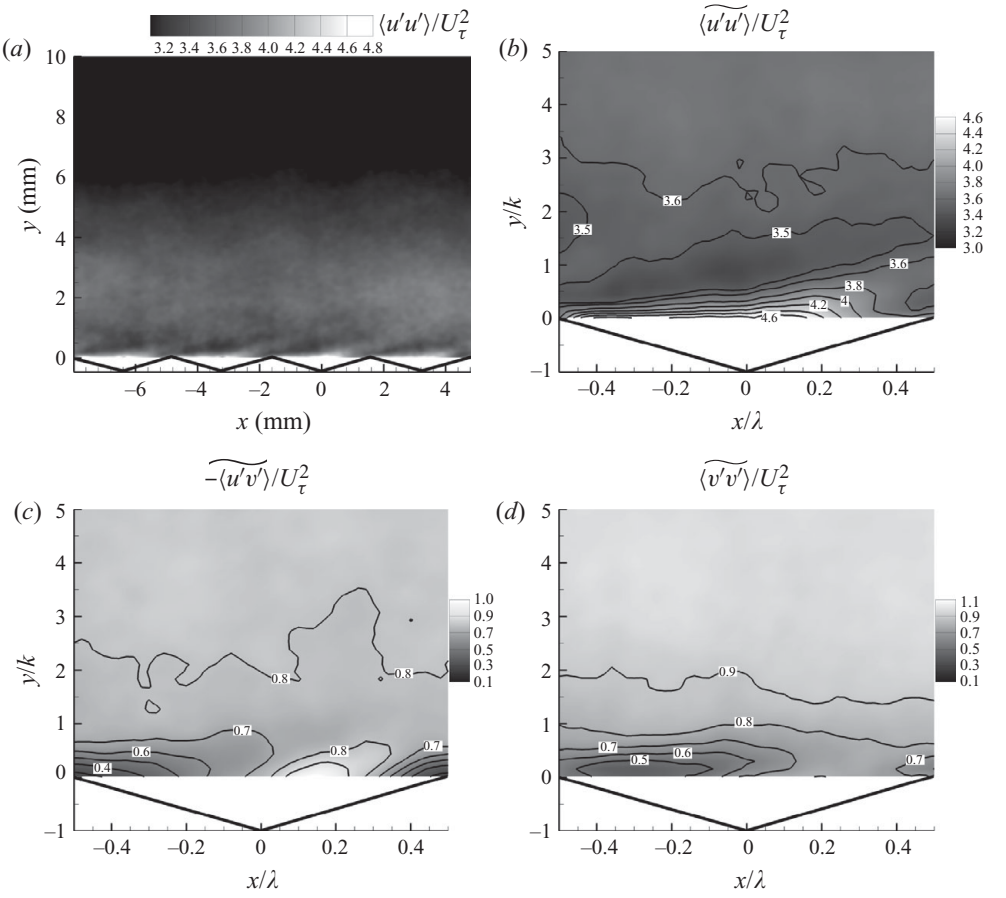

FIGURE 9. Contour plots of (*a*) $\langle u'u'\rangle$ and conditional spatial averages of Reynolds stresses: (*b*) $\widetilde{\langle u'u'\rangle}$, (*c*) $-\widetilde{\langle u'v'\rangle}$ and (*d*) $\widetilde{\langle v'v'\rangle}$ for plane 1 and $Re_\tau = 3520$.

about 10°. Extensions of both layers beyond one wavelength can be seen over the crest on the left side of figure 9(*b*). For the other two components, spatial variations are mostly limited to $y \leqslant k$. Along the backward-facing ridge, both $-\widetilde{\langle u'v'\rangle}$ and $\widetilde{\langle v'v'\rangle}$ have minima with little inclination. Their values are higher above the forward ridge, where $-\widetilde{\langle u'v'\rangle}$ peaks, and has an inclined extension that resembles the one in $\widetilde{\langle u'u'\rangle}$. The near-wall peak in $\widetilde{\langle v'v'\rangle}$ occurs slightly downstream of the other components. Similar to trends of the mean flow, spanwise periodicity in $\widetilde{\langle u'u'\rangle}$ is clearly illustrated by the x–z plane data centred at $y = 0.4k$ (figure 10*a*). The value of $\widetilde{\langle u'u'\rangle}$ is high along streamwise ridges and low in between. The peak of $\widetilde{\langle u'u'\rangle}$ above the forward ridge coincides with the region of minimal $\widetilde{U}$. Evidently, the highest values and spatial variations in $\widetilde{\langle u'u'\rangle}$ occur along the line with maximum differences in the surface protrusion. A consistent picture of the streamwise and spanwise variations in $\widetilde{\langle u'u'\rangle}$ is provided by comparing the results obtained in x–y planes 1 and 2, after spatially averaging the results over $0 < y < 0.8k$ (figure 10*b*). The near-wall distributions of Reynolds stresses change as the Reynolds number increases, even for the present limited range. At $Re_\tau = 5360$, the peak in $\widetilde{\langle u'u'\rangle}$ (figure 11*a*) is pushed

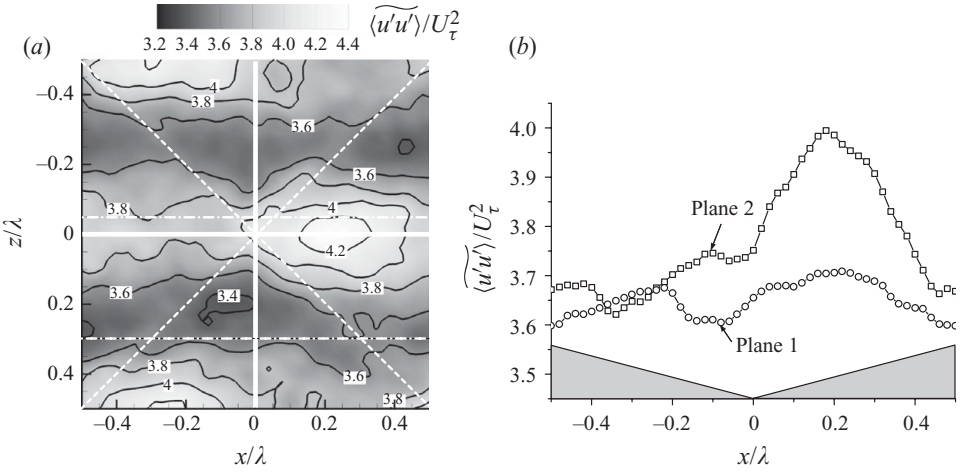

FIGURE 10. Conditionally spatially averaged Reynolds stresses at $Re_\tau = 3520$: (*a*) $\widetilde{\langle u'u'\rangle}$ contour plot at $y = 0.4k$, (*b*) $\widetilde{\langle u'u'\rangle}$ spatially averaged over $0 < y < 0.8k$ for x–y planes 1 (□) and 2 (○).

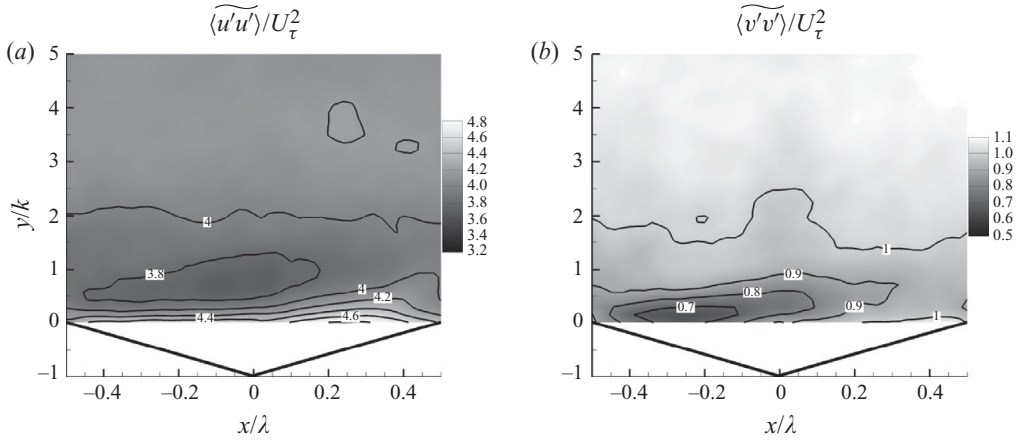

FIGURE 11. Contour plots of conditional spatially averages of Reynolds stresses: (*a*) $\widetilde{\langle u'u'\rangle}$ and (*b*) $\widetilde{\langle v'v'\rangle}$ for plane 1 and $Re_\tau = 5360$.

further downstream along the forward ridge with little variation of magnitude, while the inclination angle for the low stress layer decreases to about 7°. Accordingly, the peaks in $-\widetilde{\langle u'v'\rangle}$ (not shown) and $\widetilde{\langle v'v'\rangle}$ (figure 11*b*) also shift downstream and are located slightly downstream of the $\widetilde{\langle u'u'\rangle}$ peak.

3.2.2. *Turbulent kinetic energy budget analysis*

The TKE budget is examined using the x–y plane PIV data, but refer to the x–z plane only for validation of assumptions. For a statistically stationary turbulent flow, the TKE balance equation is (Pope 2000)

$$0 = C + T + \Pi + P + D - \varepsilon, \tag{3.1}$$

where C is the mean convection term, T is the turbulent transport, P is the production term, Π is the pressure-related term, D is the viscous diffusion, and ε is the dissipation rate. Of these terms, Π is inaccessible relying solely on velocity measurement, and D becomes important only within the viscous sublayer and insignificant in rough-wall turbulence. Approximate expressions for the spatial averages of other budget terms based on the x–y plane data are as follows:

$$\bar{C} = -\overline{U\frac{\partial k}{\partial x}} - \overline{V\frac{\partial k}{\partial y}} - \overline{W\frac{\partial k}{\partial z}} \approx 0, \tag{3.2}$$

$$\bar{P} = -\overline{\langle u_i' u_j' \rangle \frac{\partial U_i}{\partial x_j}} \approx -\overline{\langle u'v' \rangle \frac{\partial U}{\partial y}}, \tag{3.3}$$

$$\bar{T} = -\frac{1}{2}\overline{\frac{\partial \langle u_j' u_j' v' \rangle}{\partial y}} - \frac{1}{2}\overline{\frac{\partial \langle u_j' u_j' v' \rangle}{\partial z}} \approx -\frac{1}{2}\overline{\frac{\partial \langle u'u'v' \rangle}{\partial y}} - \frac{1}{2}\overline{\frac{\partial \langle v'v'v' \rangle}{\partial y}}, \tag{3.4}$$

$$\bar{\varepsilon} = \nu\overline{\left\langle \frac{\partial u_i'}{\partial x_j}\frac{\partial u_i'}{\partial x_j} \right\rangle} + \nu\frac{\partial^2 \overline{\langle u_i' u_j' \rangle}}{\partial x_i \partial x_j}, \tag{3.5}$$

$$\bar{\varepsilon}_{ASX} \approx \nu\left(-\overline{\left\langle \left(\frac{\partial u'}{\partial x}\right)^2 \right\rangle} + 8\overline{\left\langle \left(\frac{\partial v'}{\partial y}\right)^2 \right\rangle} + 2\overline{\left\langle \left(\frac{\partial u'}{\partial y}\right)^2 \right\rangle} + 2\overline{\left\langle \left(\frac{\partial v'}{\partial x}\right)^2 \right\rangle}\right), \tag{3.6}$$

$$\bar{\varepsilon}_{ISO} \approx 4\nu\left(\overline{\left\langle \left(\frac{\partial u'}{\partial x}\right)^2 \right\rangle} + \overline{\left\langle \left(\frac{\partial v'}{\partial y}\right)^2 \right\rangle} + \frac{3}{4}\overline{\left\langle \left(\frac{\partial u'}{\partial y}\right)^2 \right\rangle} + \frac{3}{4}\overline{\left\langle \left(\frac{\partial v'}{\partial x}\right)^2 \right\rangle} + \overline{\left\langle \left(\frac{\partial u'}{\partial x}\frac{\partial v'}{\partial y}\right) \right\rangle} + \frac{3}{2}\overline{\left\langle \left(\frac{\partial u'}{\partial y}\frac{\partial v'}{\partial x}\right) \right\rangle}\right). \tag{3.7}$$

The logic associated with these approximations is as follows. For the mean flow convection, spatial averaging eliminates the first term, and the experimental data show that the other two terms are about two orders of magnitude smaller than the production term. As for the turbulence production, spatial averaging eliminates the term involving $\partial/\partial x$ and the terms involving $\partial V/\partial y$ are small, leaving the mean shear term as the primary contribution. The other terms, including those measured in the x–z plane, e.g. $\overline{\langle w'w' \rangle \partial U/\partial z}$, are at least one order of magnitude smaller. Since we are predominantly concerned with wall-normal energy exchange, we only include terms available from the x–y plane data in the present study. Needless to say, the spanwise contribution might be equally significant for the turbulence transport near the wall.

To estimate the dissipation rate based only on the x–y plane measurement, one has two options. The first is to use a streamwise axisymmetric assumption, which gives $\bar{\varepsilon}_{ASX}$ shown in (3.6) (Antonia, Kim & Browne 1991). Under this assumption, the estimated ε is identical to the pseudo-dissipation, $\varepsilon_{pseudo} = \nu\langle \partial u_i'/\partial x_j,\ \partial u_j'/\partial x_i \rangle$, which appears in some DNS studies (e.g. Ikeda & Durbin 2007). A slightly different expression, $\bar{\varepsilon}_{ISO}$ shown in (3.7), is obtained by assuming local turbulence isotropy (Luznik *et al.* 2007). The validity of some of these assumptions is verified utilizing the x–z plane data. It shows that both methods provide the same good agreement for the sum of $\overline{\langle (\partial u'/\partial z)^2 \rangle}$ and $\overline{\langle (\partial w'/\partial x)^2 \rangle}$. However, the axisymmetric assumption produces a reasonable estimate for the disparity between these two terms, i.e. $\overline{\langle (\partial w'/\partial x)^2 \rangle} \approx 2\overline{\langle (\partial u'/\partial z)^2 \rangle}$. Nevertheless, based on the current data, it is still impossible to conclude which

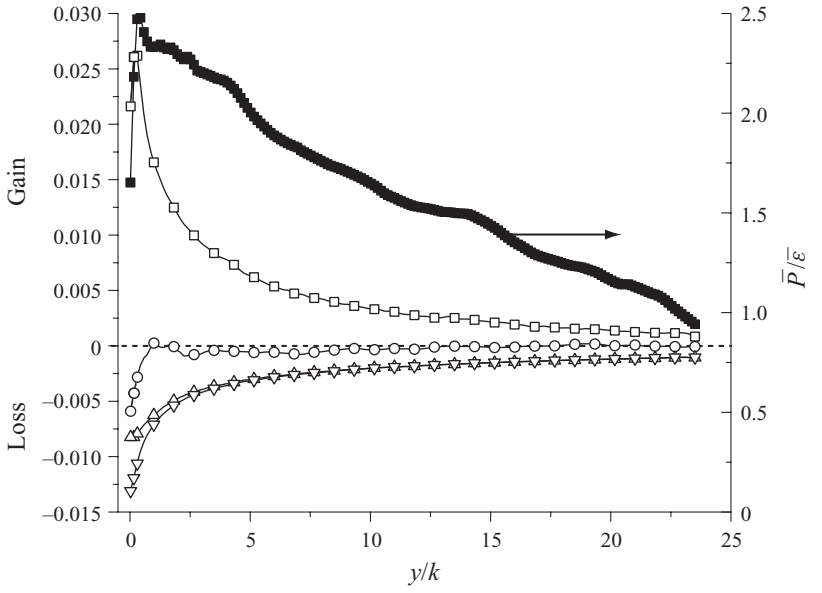

FIGURE 12. Spatially averaged TKE budget terms scaled by U_τ^4/ν for plane 1 and $Re_\tau = 3520$. Symbols: □, $\bar{P}$; ○, $\bar{T}$; △, $\bar{\varepsilon}_{AXS}$; ▽, $\bar{\varepsilon}_{ISO}$; ■, $\bar{P}/\bar{\varepsilon}_{ISO}$.

estimate provides a better near-wall approximation, so both estimates are presented in the discussion that follows. As figure 12 demonstrates, $\bar{\varepsilon}_{ASX}$ and $\bar{\varepsilon}_{ISO}$ coincide very well above the roughness sublayer, but differ near the wall. Another related issue is the effect of finite resolution of PIV data on the dissipation estimates since they are dominated by small-scale motions. The Kolmogorov scale, $\eta = (\nu^3/\varepsilon)^{1/4}$, calculated from $\bar{\varepsilon}_{ISO}$ is about 25 μm near the wall, i.e. it is significantly larger than the wall unit ∼7.1 m. Thus, our vector spacing is 2.5η and the interrogation window size is 5η near the wall, which become 1.6η and 3.2η, respectively, in the outer layer. However, the out-of-plane spatial resolution, which is estimated based on either the depth of focus of the imaging system ($\sim 12\eta$) or laser sheet thickness ($\sim 20\eta$), is lower, and consequently, has the largest impact on the attenuation of terms involved in estimates of dissipation. As discussed in the Appendix, the estimated attenuation of the dissipation rate is about 50 %. In the following analysis, we present and use the calculated dissipation rate, but one should keep in mind that its magnitude is attenuated.

Profiles of the spatially averaged estimates for the three TKE budget terms in (3.3)–(3.5) are presented in figure 12. Both production and dissipation peak in the vicinity of the roughness and decrease with increasing distance from the wall. Both terms decay sharply within the roughness sublayer, but the decay rate gradually slows down farther from the wall. The turbulent transport term also reaches maximum near the wall, but drops rapidly to almost zero within $1k$. Note that turbulent diffusion becomes slightly positive around $y = 1.7k$, indicating that energy is transported into this domain from neighbouring areas. In the rest of the flow domain, turbulence diffusion is negative. All the three calculated terms contribute significantly to the TKE balance at $y < k$, while production and dissipation become the only dominant terms at higher elevations. The ratio of production to dissipation $\bar{P}/\bar{\varepsilon}$ (where $\bar{\varepsilon}_{ISO}$ is used to represent ε) is also plotted in figure 12 to illustrate their relative contributions across the channel, although $\bar{\varepsilon}_{ISO}$ is most likely underestimated. As is evident, $\bar{P}/\bar{\varepsilon}$

peaks very near the wall, where most of turbulence is produced, and the surplus TKE must be transported away, consistent with the high local wall-normal transport. This ratio and the turbulent transport decrease rapidly, even within $y < k$. Further above, $\bar{P}/\bar{\varepsilon}$ keeps on decreasing, initially at a low rate (up to $y \approx 4k$), and then at a faster pace with increasing elevation. The magnitude of $\bar{P}/\bar{\varepsilon}$ falls below 1 at $y \approx 21k$. However, due to the attenuation of ε discussed earlier, the elevation where dissipation surpasses the production can be expected to be much closer to the wall. In spite of this concern, some of the present trends are consistent with the DNS results for the two-dimensional rough-wall channel flow (e.g. Ikeda & Durbin 2007). In Ikeda & Durbin (2007), they indicate that local maxima in $\bar{P}/\bar{\varepsilon}$ coincide with those of $\overline{\langle u'u' \rangle}$. The first peak is located near the roughness, and the second one, much broader, appears at $y \approx 3k$. In our data, the $\overline{\langle u'u' \rangle}$ upsurge near the wall is affiliated with the $\bar{P}/\bar{\varepsilon}$ peak there. Although $\bar{P}/\bar{\varepsilon}$ does not have a second maximum in our case, its decay rate is slow up to $y \approx 4k$, which coincides the region where $\overline{\langle u'u' \rangle}$ has a broad maximum. The faster decay of $\bar{P}/\bar{\varepsilon}$ at higher elevations indicates an increasing impact of local dissipation on the turbulence budget.

Within the roughness sublayer, spatial variations of each TKE budget term become appreciable. Selected contour plots of in-plane contributions to conditional spatial averages of several terms associated with turbulence production are illustrated in figure 13. Their definitions are as follows:

$$\widetilde{P_{uu}^{2D}} = -2(\widetilde{\langle u'u' \rangle \partial U/\partial x} + \widetilde{\langle u'v' \rangle \partial U/\partial y}), \tag{3.8}$$

$$\widetilde{P_{vv}^{2D}} = -2(\widetilde{\langle u'v' \rangle \partial V/\partial x} + \widetilde{\langle v'v' \rangle \partial V/\partial y}), \tag{3.9}$$

$$\widetilde{P^{2D}} = 0.5\big(\widetilde{P_{uu}^{2D}} + \widetilde{P_{vv}^{2D}}\big), \tag{3.10}$$

where $\widetilde{P_{uu}^{2D}}$, $\widetilde{P_{vv}^{2D}}$ and $\widetilde{P^{2D}}$ represent conditional spatial averages of $\langle u'u' \rangle$, $\langle v'v' \rangle$ and the TKE production, respectively. It is evident that except for a factor of 2, the distributions of $\widetilde{P_{uu}^{2D}}$ and $\widetilde{P^{2D}}$ (figures 13*a* and 13*c*, respectively) have very similar pattern, and peak at the same location as the $\widetilde{\langle u'u' \rangle}$ maximum. As demonstrated in figure 13(*d*), which displays P^{2D} averaged over $0 < y < 0.8k$, the spatial variations in $\widetilde{P^{2D}}$ are mainly caused by $-\widetilde{\langle u'u' \rangle \partial U/\partial x}$. The largest term, $-\widetilde{\langle u'v' \rangle \partial U/\partial y}$, contributes significantly to the magnitude of $\widetilde{P^{2D}}$, but remains relatively uniform across the span of the roughness wavelength. The third term, $-\widetilde{\langle v'v' \rangle \partial V/\partial y}$, is very small for the most part, and $-\widetilde{\langle u'v' \rangle \partial V/\partial x}$ (not shown) is negligible everywhere. Note that the in-plane contributions to the TKE production account for most of the overall TKE production rate since the out-of-plane contribution is at most $\sim 10\,\%$ of the in-plane values based on the analysis of the x–z plane data. The peaks in $\widetilde{\langle u'u' \rangle}$ and overall production above the forward face are associated with deceleration of the streamwise velocity. As for the wall-normal component, the spatially averaged $\langle v'v' \rangle$ production is almost zero, indicating that the magnitude of $\langle v'v' \rangle$ is dominated by the inter-component energy transfer. However, the spatial variation of the $\langle v'v' \rangle$ production (figure 13*b*) seems to be sufficiently large to affect local velocity fluctuations. Near the wall, it is negative above a large portion of λ and becomes positive just upstream of the crest, consistent with the patterns of high and low regions in $\langle v'v' \rangle$.

The dissipation (figure 14*a*) appears to be distributed more evenly in comparison to the production rate, with low values in the vicinity of the crest and trough, and broad maxima between them, slightly downstream of the production maxima. Its

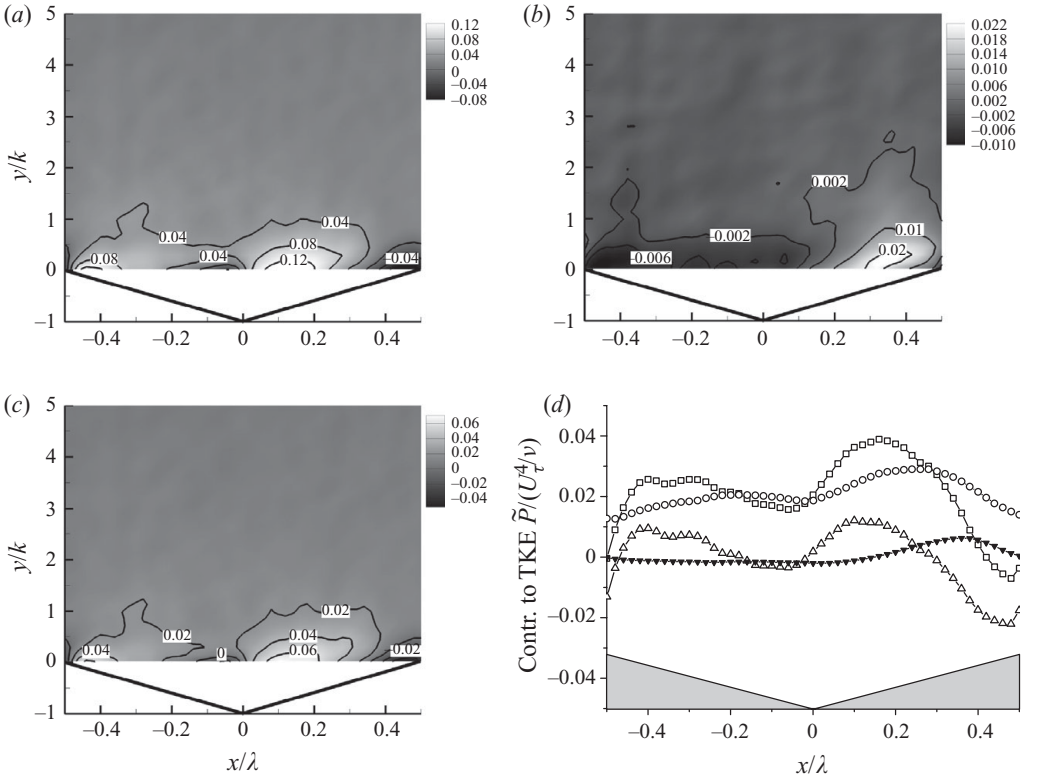

FIGURE 13. Near-wall spatial variations of x–y plane contributions to (*a*) $\langle u'u' \rangle$ production, (*b*) $\langle v'v' \rangle$ production and (*c*) TKE production. (*d*) A comparison among terms contributing to the TKE production, spatially averaged over $0 < y < 0.8k$. Symbols: □, total in-plane TKE production; ○, $-\widetilde{\langle u'v' \rangle \partial U/\partial y}$; △, $-\widetilde{\langle u'u' \rangle \partial U/\partial x}$; ▼, $-\widetilde{\langle v'v' \rangle \partial V/\partial y}$.

spatial variability diminishes at $y > k$. In the distribution of the wall-normal turbulent transport, i.e. $\widetilde{T} = 0.5 \times (\partial \widetilde{\langle u'u'v' \rangle}/\partial y + \partial \widetilde{\langle v'v'v' \rangle}/\partial y)$ (figure 14*b*), the negative peak where energy is depleted is located downstream of the maximum in the TKE production. Contours of both contributors to $\widetilde{T}$ (not shown individually) exhibit shallowly inclined patterns and consist of adjacent layers with positive and negative signs. The angles and wall-normal extent of these layers are similar to those observed in the plots of $\langle u'u' \rangle$. The major contributor in the streamwise turbulent transport, $0.5 \times \partial \widetilde{\langle u'u'u' \rangle}/\partial x$ (not shown), has a negative peak at the same location as that of the $\langle u'u' \rangle$ maximum. We also provide the distribution of $\widetilde{\langle u'u'v' \rangle}$ in figure 14(*c*), which displays an inclined positive layer extending from above the trough, coinciding with the patterns in $\langle u'u' \rangle$.

The confinement of spatial variability in turbulence statistics to the roughness sublayer can be explained by investigating the quadrant contribution to these quantities. The flow field is decomposed into four quadrants based on the orientation of the velocity fluctuation vectors, namely, upward motion (Q1: $u' > 0$, $v' > 0$), ejection (Q2: $u' < 0$, $v' > 0$), downward motion (Q3: $u' < 0$, $v' < 0$) and sweep (Q4: $u' > 0$, $v' < 0$). Figure 15 shows the contribution of each quadrant to the Reynolds shear stress with increasing distance from the wall. Ejections and sweeps are dominant everywhere, as expected, with higher contributions from sweep very near the wall

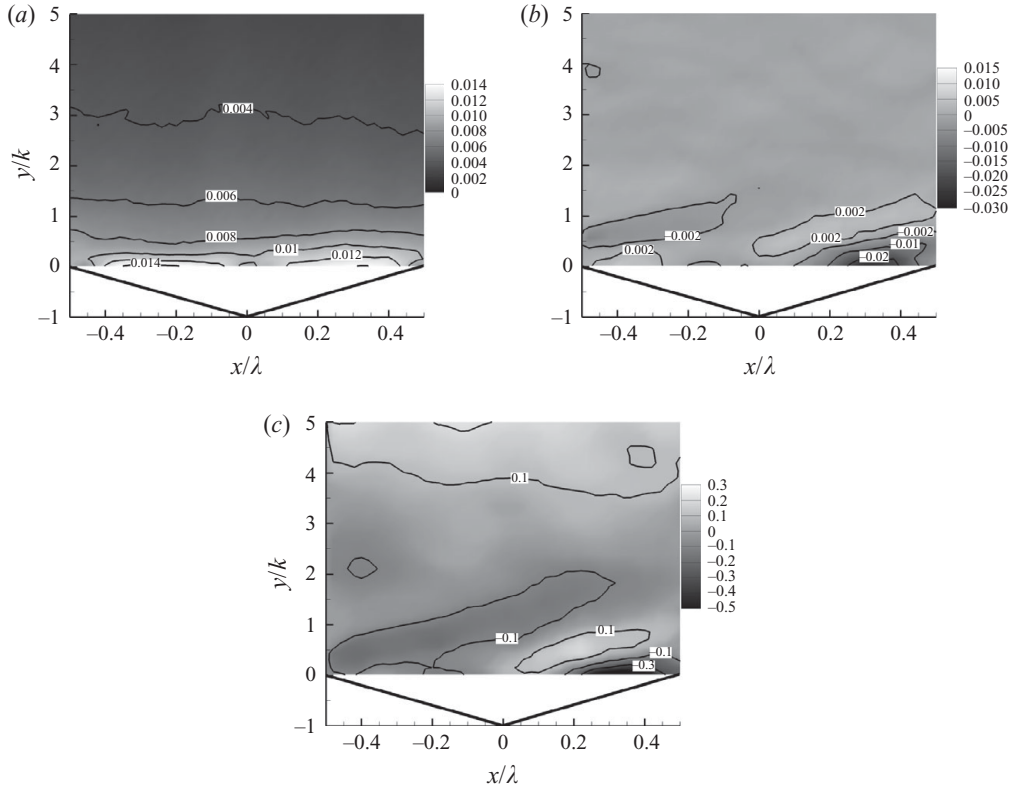

FIGURE 14. Near-wall spatial variations of (*a*) $\tilde{\varepsilon}_{ISO}/(U_\tau^4/\nu)$, (*b*) $\widetilde{T}/(U_\tau^4/\nu)$ and (*c*) $\widetilde{\langle u'u'v'\rangle}/U_\tau^3$ for x–y plane 1 and $Re_\tau = 3520$.

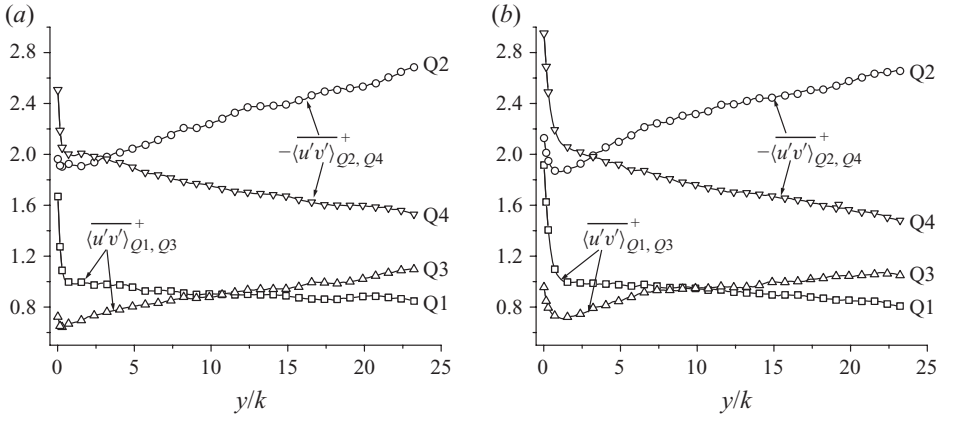

FIGURE 15. Quadrant contributions to the Reynolds shear stress (note the differences in signs) scaled by $-\overline{\langle u'v'\rangle}$ (denoted by a superscript '+') at corresponding elevations for (*a*) $Re_\tau = 3520$ and (*b*) $Re_\tau = 5360$. Symbols: □, Q1; ○, Q2; △, Q3; ▽, Q4.

and from ejection above $y \approx 3k$. Nevertheless, it is of note that a significant amount of negative Q1 contribution is evident adjacent to the roughness with a magnitude close to that of Q2. The contour plots of quadrant-sampled $\widetilde{\langle u'u'\rangle}$ show that spatial

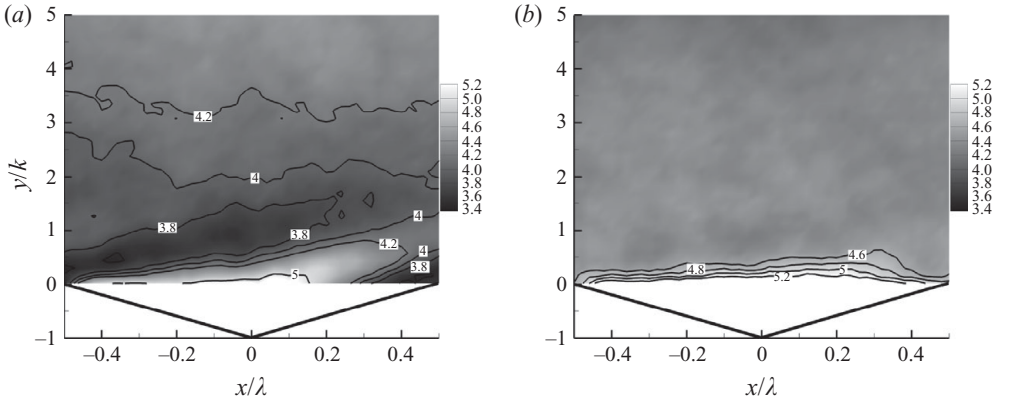

FIGURE 16. Quadrant contributions of (*a*) Q2 and (*b*) Q4 events to $\widetilde{\langle u'u'\rangle}/U_\tau^2$ for x–y plane 1 and $Re_\tau = 3520$.

variations in $\widetilde{\langle u'u'\rangle}$ occur primarily during ejection events (figure 16*a*), while the contribution of sweeps remains almost uniform (figure 16*b*). Decompositions of other turbulence quantities (not shown) also support that ejections are responsible for most of inclined patterns extending upward, while sweep contributions are more equally distributed with higher magnitudes close to the wall. For instance, in the $\widetilde{\langle u'u'v'\rangle}$ contour (figure 14*c*), the inclined, high positive layer is generated by ejections, while the broad negative region above the forward face is mainly due to sweeps. Such trends are expected since ejections carry structures produced within and near the roughness away from the wall while sweeps squeeze them into the vicinity of roughness, as demonstrated by Zhu, van Hout & Katz (2007) for canopy flows. In the resulting thinner shear layer during sweeps, both the Reynolds shear stress and strain rate are higher. Consequently, the TKE production rate during sweep events is larger than that during ejections in the roughness sublayer, especially below $y \approx k$ for our case. Although weaker ejections subsequently lift up the turbulence which contains its spatial variability, the confined production limits the spatial non-uniformity in turbulence statistics below $y \approx 2k$. As the Reynolds number increases, the contribution of sweeps to shear stress (figure 15*b*) increases near the wall, but the size of the region where sweeps dominate varies very little.

3.3. *Flow structures in the roughness sublayer and regions above*

3.3.1. *Spatial energy spectra*

Spatial energy spectra $E_{11}(k_1)$, $E_{22}(k_1)$ and shear spectra $E_{12}(k_1)$ are calculated along streamwise lines of instantaneous data and then ensemble-averaged, where subscripts 1 and 2 refer to the streamwise and wall-normal velocity components. We apply fast Fourier transform (FFT) without any other windowing function except for removing the mean value and linear detrending. The spectra presented are scaled in two ways for different purposes. First, as shown in figure 17, we scale each spectrum with the spatially averaged Reynolds stress at the corresponding elevation, which keeps both horizontal and vertical axes dimensional. This scaling accentuates subtle variations in spectral shapes with increasing distance from the wall, and is convenient to compare variation in energy distributions at the same physical length scales. The other way of scaling refers to compensated energy spectra (figure 18), namely $E_{ii}(k_1)\varepsilon^{-2/3}k_1^{5/3}$ plotted against $k_1\eta$, with the Kolmogorov scale estimated based on $\bar{\varepsilon}$ at corresponding

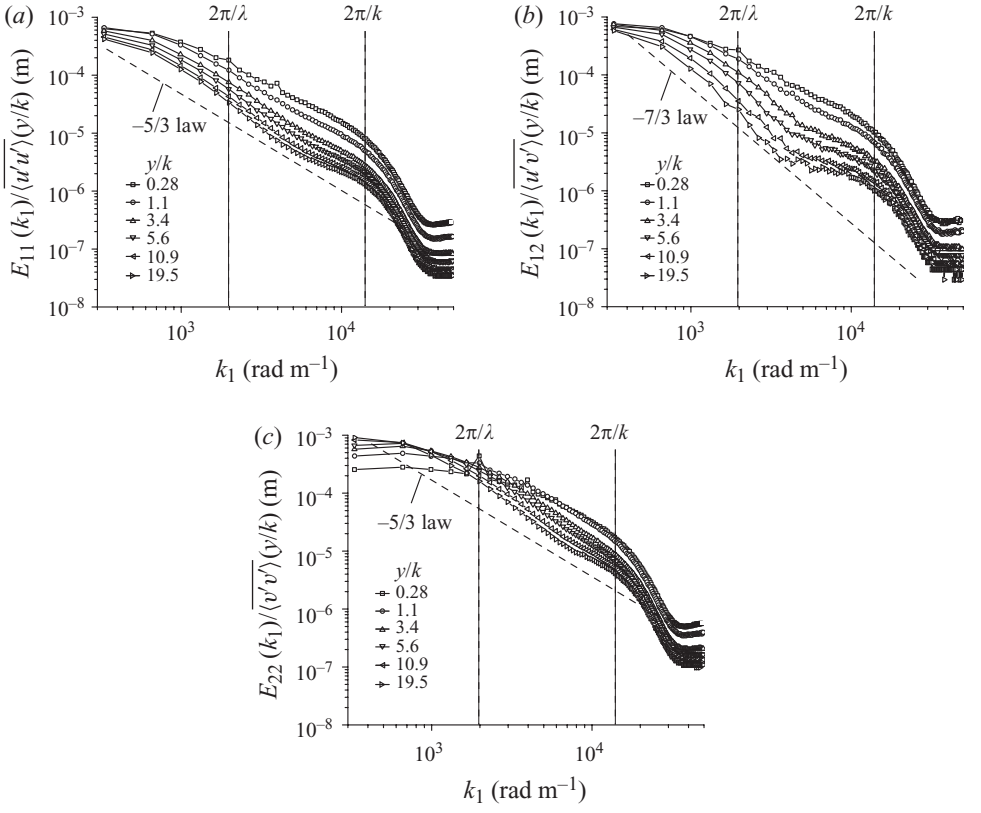

FIGURE 17. Spatial spectra for x–y plane 1 and $Re_\tau = 3520$: (*a*) $E_{11}(k_1)/\overline{\langle u'u'\rangle}$, (*b*) $E_{12}(k_1)/-\overline{\langle u'v'\rangle}$ and (*c*) $E_{22}(k_1)/\overline{\langle v'v'\rangle}$.

elevations. Since $\bar{\varepsilon}$ decays with increasing elevation, i.e. η increases, values of $k_1\eta$ equivalent to a certain length scale, e.g. k and λ, also increase with elevation. Therefore, we highlight the points corresponding to k and λ in each plot (figure 18) for better reference. Using this scaling, an inertial range spectrum is represented as a horizontal line, which intercepts the vertical axis at $E_{11}(k_1)\varepsilon^{-2/3}k_1^{5/3} = 0.49$ and $E_{22}(k_1)\varepsilon^{-2/3}k_1^{5/3} = 0.65$ ($E_{22}(k_1)/E_{11}(k_1) = 4/3$) in isotropic turbulence and in the outer parts of high-Reynolds-number turbulent boundary layers (Saddoughi & Veeravalli 1994). These expected values are indicated by horizontal dashed lines in figure 18. Before discussing the trends, note that due to the finite spatial resolution of the PIV data, the spectral energy is attenuated significantly up to scales of several times the interrogation window size (Zhu & Antonia 1996; Lavoie *et al.* 2007; Hackett *et al.* 2009). The depth of the sample volume also affects the spectra along with the dissipation rate, as discussed and demonstrated in the Appendix.

Several trends can be observed in the dimensional energy and shear spectra (figure 17). First, as expected, spatial variation in the flow within the roughness sublayer generates spectral peaks at $k_1 = 2\pi/\lambda$ and its multiples, representing the effects of the periodic flow patterns imposed by the roughness. These peaks disappear at higher elevations, consistent with the data presented earlier. Second, at low wavenumbers, all the spectra steepen with increasing distance from the wall, demonstrating a growing contribution of large-scale turbulence and a decreasing role

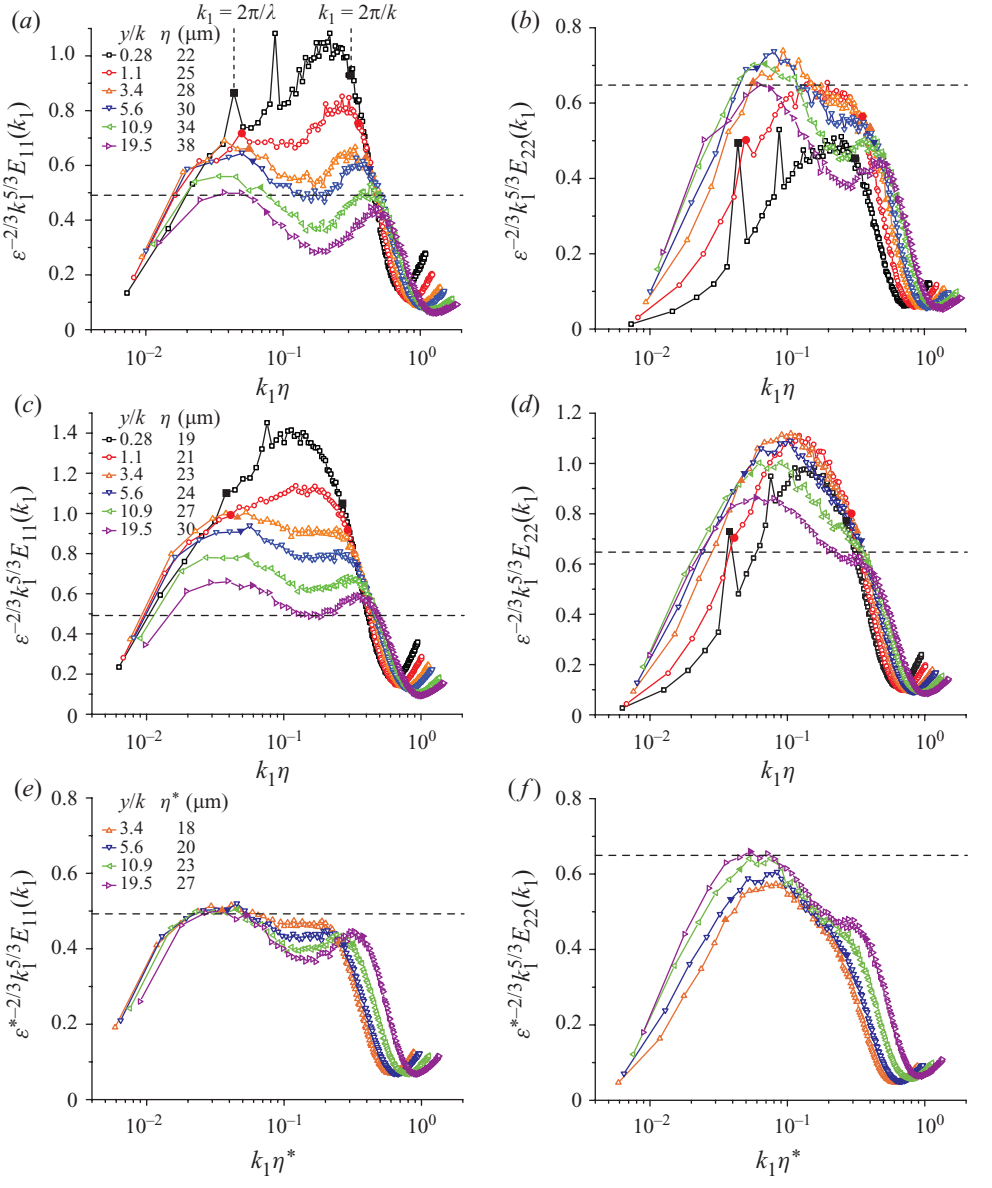

FIGURE 18. Compensated energy spectra in x–y plane 1, with magnified solid symbols marking wavenumbers corresponding to λ and k: (*a*) $E_{11}(k_1)$, $Re_\tau = 3520$; (*b*) $E_{22}(k_1)$, $Re_\tau = 3520$; (*c*) $E_{11}(k_1)$, $Re_\tau = 5360$; (*d*) $E_{22}(k_1)$, $Re_\tau = 5360$. In (*e*) and (*f*) we re-plot the data in (*c*) and (*d*), respectively, using dissipation rates that match the compensated $E_{11}(k_1)$ at $k_1\eta^* \approx 0.3$ with constants expected in Kolmogorov inertial-range spectra.

of small-scale energy. Third, at low wavenumbers, the shear spectra show a tendency towards a $-7/3$ slope, the expected slope for the inertial range shear-stress spectrum (Lumley 1967), with increasing distance from the wall. For the same wavenumber range, the slope of $E_{11}(k_1)$ approaches $-5/3$. Finally, for wavelengths in the k–$3k$ range, all the spectra flatten, i.e. display a decrease in slope magnitude outside of the

roughness sublayer. This pattern is most pronounced in the $E_{12}(k_1)$ plots and least in $E_{22}(k_1)$.

In the corresponding compensated spectra (figures 18*a* and 18*b*), the flattening pattern appears as a distinct bump in the same wavenumber range. It occurs at all elevations including well above the roughness sublayer, indicating the presence of excessive energy at this scale range. In general, the entire compensated $E_{11}(k_1)$ decreases rapidly with elevation with a particularly fast decay rate around the high wavenumber bump. For compensated $E_{22}(k_1)$, the corresponding bump is low very near the wall in accordance with the entire spectrum. It reaches a maximum value within the roughness sublayer, and then decreases with further increase in elevation. At higher elevations above the roughness sublayer, it is noticeable that another peak forms at low wavenumbers of the compensated $E_{11}(k_1)$ in the vicinity of $k_1\eta \sim 0.04$ and its magnitude also decreases with elevation. Similarly, the low wavenumber bump is also observed in the compensated $E_{22}(k_1)$ but only at $y > 3.4k$, i.e. above the peak in the corresponding Reynolds stress. Since the magnitudes of both $E_{11}(k_1)$ and $E_{22}(k_1)$ near the low wavenumber peak have expected inertial range values (Pope 2000), the presence of these low wavenumber bumps suggests that an inertial range is beginning to form with increasing distance from the wall.

With increasing Reynolds number (figures 18*c* and 18*d*), although formation of two compensated $E_{11}(k_1)$ peaks occurs at higher elevations, spectral bumps at scales of k–$3k$ are still evident. In the $0.02 < k_1\eta < 0.07$ range, a broad peak begins to form at and above $y = 3.4k$, with a higher compensated value than those measured at the lower Reynolds numbers. This trend may be related to the increasing attenuation of the dissipation rates as the Reynolds number increases and the Kolmogorov scale decreases. Therefore, we re-scale the compensated spectra at the four highest elevations using adjusted dissipation rates ($\varepsilon*$), which bring the compensated value of $E_{11}(k_1)$ at the broad peak to the constant of the Kolmogorov inertial range spectrum. The same $\varepsilon*$ is also adopted for scaling $E_{22}(k_1)$ and recalculating the Kolmogorov scale ($\eta*$). The results are presented in figures 18(*e*) and 18(*f*), along with values of $\eta*$ at each elevation. After rescaling, the compensated $E_{11}(k_1)$ collapse at all scales larger than λ. Values of the compensated $E_{22}(k_1)$ still increase slightly with elevation in this wavenumber range, but reach the expected Kolmogorov inertial range at the two highest elevations and expected larger wavenumbers. These trends suggest the establishment of a Kolmogorov-cascading process in the outer layer. The same process and conclusions can be found by rescaling the spectra at the lower Reynolds number. In this case, the required corrections to the magnitude of dissipation rate vary between 0 and 50 %, in agreement with the range of estimated attenuation in dissipation discussed in the Appendix. However, in spite of this uncertainty and attenuation of small-scale energy due to the finite resolution of PIV data, the existence of excessive energy at scales close to k is clearly evident. We conjecture that this excessive energy is a result of generation of eddies with a typical roughness scale in the vicinity of the rough surface. These eddies are subsequently advected away from the wall by large-scale turbulent structures that populate the outer layer of the channel.

To demonstrate this phenomenon, figure 19(*a*) shows an instantaneous velocity and vorticity distribution after subtracting $0.5U_c$ from each vector. An inclined large-scale structure is clearly observed across the entire flow domain at $y > 5k$, whose two-dimensional signature resembles the hairpin structures studied by Adrian's group (e.g. Adrian *et al.* 2000). The region below this structure is populated with small-scale eddies. Adjacent to the roughness, the flow contains several inclined trains of vortices. To examine the spatial distribution of roughness-scale eddies, we spatially

https://doi.org/10.1017/S0022112010003988 Published online by Cambridge University Press

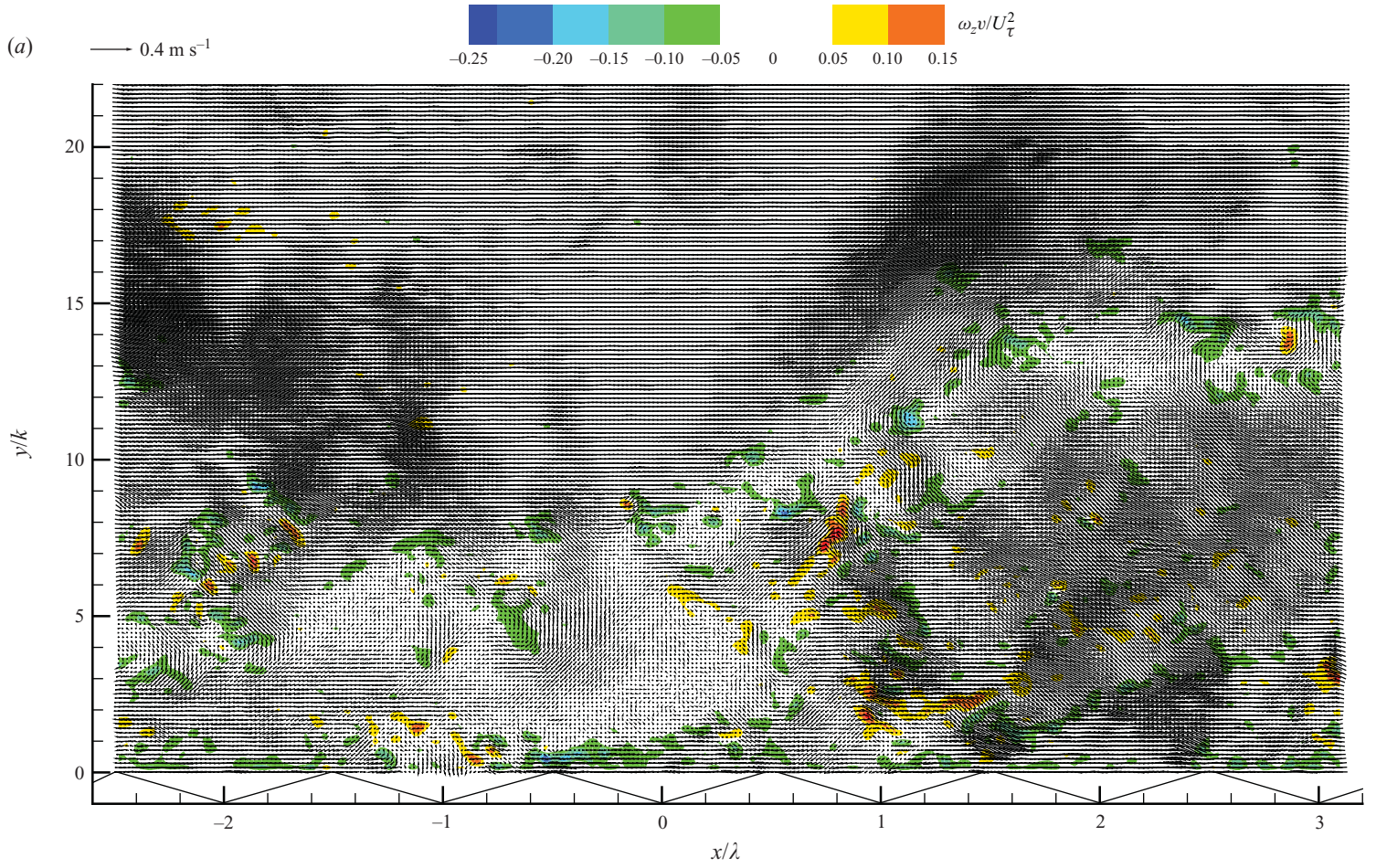

FIGURE 19. For caption see next page.

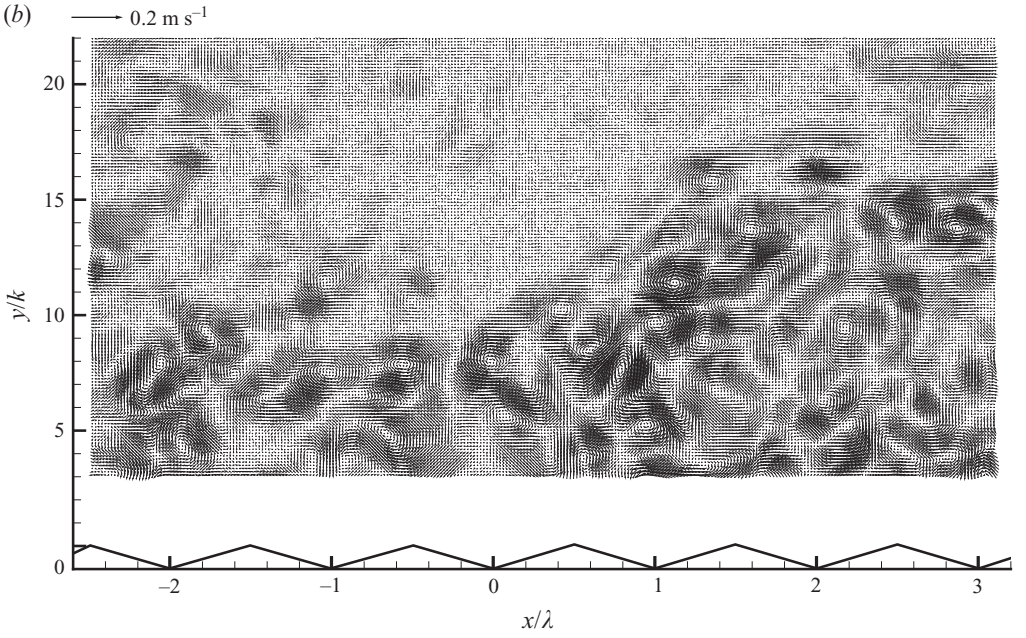

FIGURE 19. (*a*) (See hi-res example online as supplementary material at journals.cambridge.org/flm) Sample instantaneous velocity distribution for x–y plane 1 and $Re_\tau = 3520$, after subtracting $0.5U_c$ from each vector. Colours indicate the scaled vorticity. (*b*) The same velocity field, spatially bandpass-filtered using box filters in the k–$3k$ range.

bandpass-filter this velocity distribution by calculating the two-dimensional box-filtered vector maps at scales k and $3k$, and subtracting them from each other. The resulting instantaneous velocity map is presented in figure 19(*b*). Evidently, the entire field is filled with eddies in the k–$3k$ size range. In general, the eddy strength diminishes with increasing elevation, but there is a clear separation below and above the shear layer interface, marking the in-plane signature of large-scale structures. Below this interface, the stronger structures are observed and they appear to be 'newborn' eddies that have just been entrained from the wall by the large structures. While above, the eddies are relatively weak, presumably since they were entrained at earlier times and have been partially dissipated. Similar patterns with variations in size and location are present in numerous velocity distributions that we have examined, indicating that the anecdotal evidence shown here is a regularly occurring phenomenon. This rapid wall-normal transport of roughness-scale eddies induces the excessive energy at the same scales in all the energy spectra. The time scales associated with this transport are not long enough for these eddies to dissipate and, consequently, they leave imprints in the spectra across the entire flow domain. Clearly, these eddies are not produced by the typical energy-cascading process of turbulence at large scales, and hence lead to distinct bumps in the compensated spectra (figure 18). The resulting excessive energy in the 15η–30η scale range should enhance the dissipation rate since it is located in the most dissipative range in isotropic turbulence (Pope 2000). Such an expectation is consistent with the trend of P/ε above the roughness sublayer.

Several relevant comments should be made before concluding this section. First, spectra of PIV data obtained in a number of measurements performed in the coastal-ocean bottom boundary layer also exhibit bumps (e.g. Nimmo Smith, Katz & Osborn 2005; Luznik *et al.* 2007). In Nimmo Smith, Katz & Osborn (2005), we verified

that these bumps are not an artefact of the measurement or analysis procedures by applying the same codes (PIV analysis and spectral calculations) to process laboratory isotropic turbulence data and confirming that they do not have bumps. In support of our claims, Hackett *et al.* (2010) show that the length scale associated with the oceanic bumps, ~ 2 cm, is very different from the present scales, but matches the local height of bottom ripples. Second, spectral bumps have been observed in a few canopy flow studies (e.g. Seniger *et al.* 1976), where they have been commonly related to the interactions of large-scale motion with canopy elements (e.g. Finnigan 2000). Third, bumps also exist in the spectra of hot-wire data obtained in the atmospheric boundary layers (Champagne *et al.* 1977) and high-Reynolds-number wind tunnel boundary layers (Saddoughi & Verravalli 1994). In both cases, the authors do not relate this phenomenon to specific flow features, but others have attributed the bumps to an energy bottleneck at the transition between inertial and dissipation ranges (e.g. Falkovich 1994). Recently obtained spectra within smooth-wall boundary layers (e.g. Mathis, Hutchins & Marusic 2009) show that small-scale turbulence dominates near the surface, but decays and eventually disappears with increasing distance from the wall. A second, distinctly lower-wavenumber peak forms away from the wall. The present rough-wall data also show that a low wavenumber peak develops away from the wall, but the distinct signature of the small-scale turbulence persists over the entire boundary layer. Finally, the particularly large signature of roughness-scale eddies in the shear spectra (figure 17*b*) is a further manifestation of their role in the wall-normal momentum transport. Incidentally, in the compensated shear spectra (not shown), the peak is centred on the wavenumber corresponding to the roughness height.

3.3.2. *Analysis of flow structures based on LSE*

To statistically investigate the mechanisms dominating vortex lifting, we apply the swirling strength-based LSE at different elevations to obtain the conditionally averaged velocity fields, as introduced in § 2. Sample results are presented in figure 20, with a solid circle marking the location of the swirling strength condition. We opt to retain the relative length of each vector to highlight the significant flow features since the domain contains numerous very weak structures, whose enhancement by normalization may introduce unreal physical patterns. Furthermore, to increase statistical convergence in results obtained at $y < 2.5k$ (only), we also apply conditional spatial averaging of data obtained at corresponding locations relative to the roughness. This procedure generates smoother vector fields but has little effect on the flow features. For a swirl at $y = 1.4k$ (figure 20*a*), a clockwise vortex is centred at the event location with strong ejection upstream and below. The characteristic size of this vortex is k–$2k$, as can be quantitatively confirmed based on the two-point correlations of λ_{2D} and velocity fluctuations (not shown). Sweep events are observed above and upstream of this vortex. Downstream of the vortex, the flow contains a series of weak vortical patterns at approximately the same elevation. Data obtained for events at the same elevation but different streamwise locations show similar trends, with some variations in the relative magnitude of vectors surrounding the event points. For swirl events located below $1k$ (not shown), the only discernible flow feature is a clockwise-rotating vortex with a sweeping flow above.

For events occurring at $y \approx 2.5k$ (figure 20*b*), a distinct shear layer shown by a dashed line becomes visible in the neighbourhood of the event, with sweep above and ejection below. It has a slight upward inclination upstream of the event, but becomes horizontal downstream. At this elevation, the coherent pattern disappears beyond about one wavelength on both sides of the event. At $y = 6.3k$ (figure 20*c*), the inclined

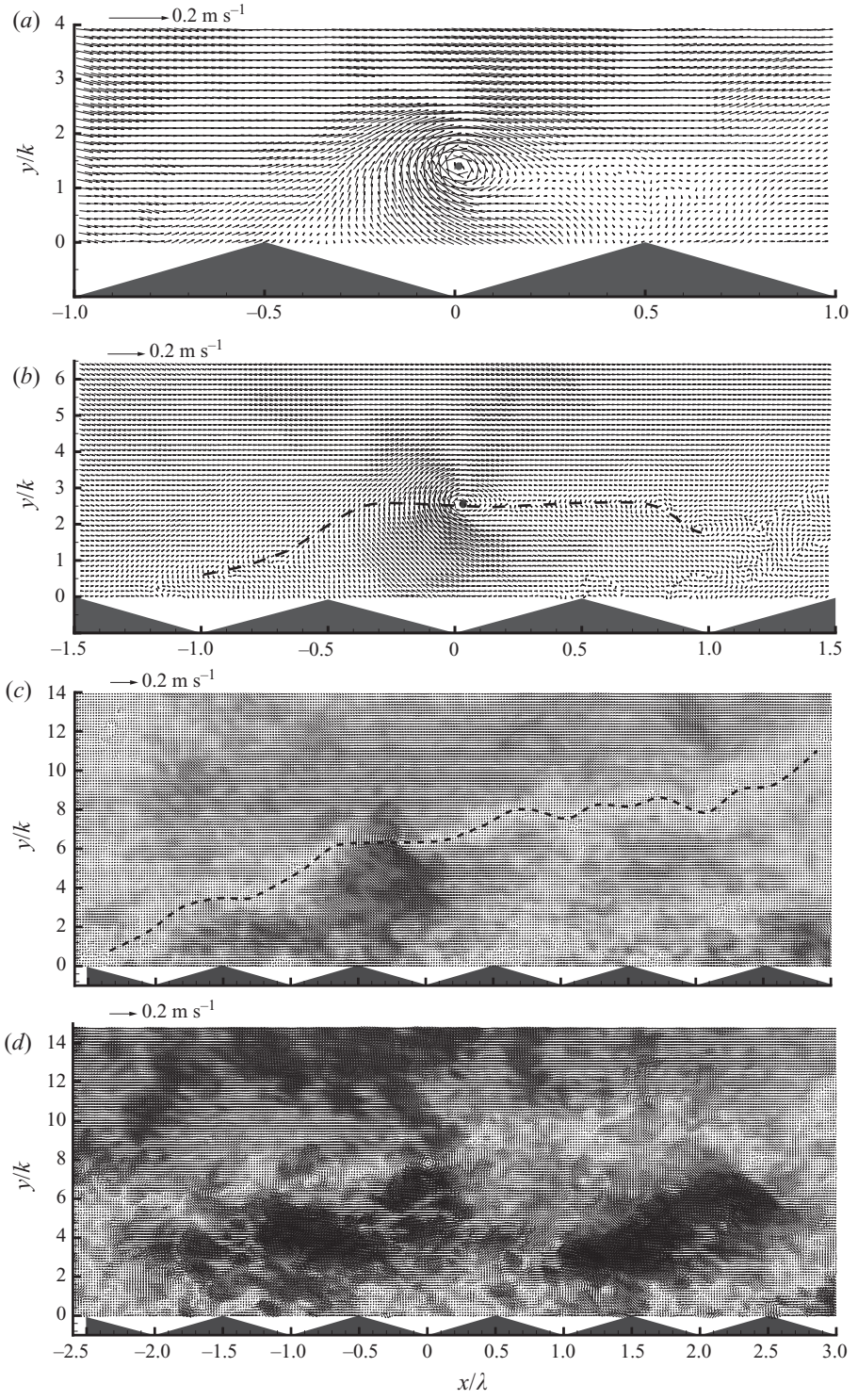

FIGURE 20. LSE of vector fields based on the swirling strength at (*a*) $y = 1.4k$, (*b*) $y = 2.5k$, (*c*) $y = 6.3k$ and (*d*) $y = 7.6k$ (shown by solid dots) for x–y plane 1 and $Re_\tau = 3520$. Dashed lines in (*b*) and (*c*) mark the location of shear layers.

shear layer becomes clearly evident. It contains a train of vortices with scale of k–$2k$ separating regions of sweep and ejection. At this elevation, the shear layer extends over the entire sample area and qualitatively resembles the instantaneous sample in figure 19(*a*). Formation of shear layers has been reported before in boundary layers over both smooth and rough walls analysed using LSE (e.g. Christensen & Adrian 2001; Volino *et al.* 2009). On the basis of an investigation of experimental and computational data, Adrian's group (e.g. Adrian *et al.* 2000; Christensen & Adrian 2001) has attributed this phenomenon to the flow induced by hairpin vortex packets. In their results, the spacing between vortex cores along the shear layer (hairpin heads) is of the same order as their distance from the wall. Although in the present rough-wall case, the shear layer is populated with more tightly packed roughness-scale eddies, the overall feature appears to be similar, including the formation of features separated by a distance that is close to the local elevation.

At $y = 7.6k$, in addition to the phenomena described above, a pair of strong ejection regions highlights the presence of two large structures, each inclined at $\sim 45^\circ$, and each with a spanwise vortex at its highest, most downstream point. Their streamwise extent, 2λ–2.5λ, is considerably larger than the roughness wavelength or the distance from the wall. This scale approximately corresponds to that of the low wavenumber peak in the compensated energy spectra (figure 18), i.e. the streamwise integral scale. As shown in § 3.3.1, eddies of such scales exhibit inertial range characteristics and are involved in an energy-cascading process that is eventually disrupted by roughness-scale eddies. Although we cannot determine how these structures are produced based on the present data, their persistent quasi-periodic appearance suggests that they are related. At higher elevations, the distinct shear layer becomes less visible in the original LSE plots, but the 'blobs' of the strong ejection region remain over the entire domain of the high-resolution measurement. However, upon low-pass filtering of the data, which removes the swirling strength peaks associated with roughness-scale eddies, the shear layer clearly reappears (not shown).

In summary, the LSE-based analysis indicates that at $y < 1.5k$, the flow field is dominated by roughness-scale eddies. Although the instantaneous data frequently show inclined trains of vortical structures (e.g. figure 19), there is no statistical evidence of spatial coherence that would suggest the formation of small-scale hairpin packets. A shear layer with at least roughness wavelength-scale coherence, implying correlated vortex trains, appears only from $y \approx 2.5k$. Within the logarithmic layer, the shear layer has features that resemble those induced by hairpin packets in prior studies (e.g. Christensen & Adrian 2001). Quasi-periodic structures, consisting of strong ejection events, emerge at higher elevation and have integral length scales. Nevertheless, the flow field is still flooded with roughness-scale eddies.

Imprints of some of the aforementioned flow structures can also be seen in the distributions of two-point spatial correlations. Sample R_{uu} and R_{vv} during Q2 and Q4 events, denoted as $R_{uu,Qi}$, at several elevations are presented in figure 21. As seen in numerous prior studies (e.g. Krogstad & Antonia 1994; Volino *et al.* 2009), R_{uu} has a much longer extent than R_{vv}, especially in the streamwise direction. The differences between R_{uu} and R_{vv} are explained by Adrian (2007) based on the hairpin packet model. For correlation coefficients below 0.7, the R_{uu} contours are inclined at shallow angles, whose orientations agree with the inclination of the shear layer in the LSE results, as well as the train of vortices demonstrated in instantaneous realizations. This inclination diminishes for higher correlation values, but contours remain elliptical, consistent with the shape of the vortex at the event point of the LSE data. Correlations associated with sweeps have larger extent than those with

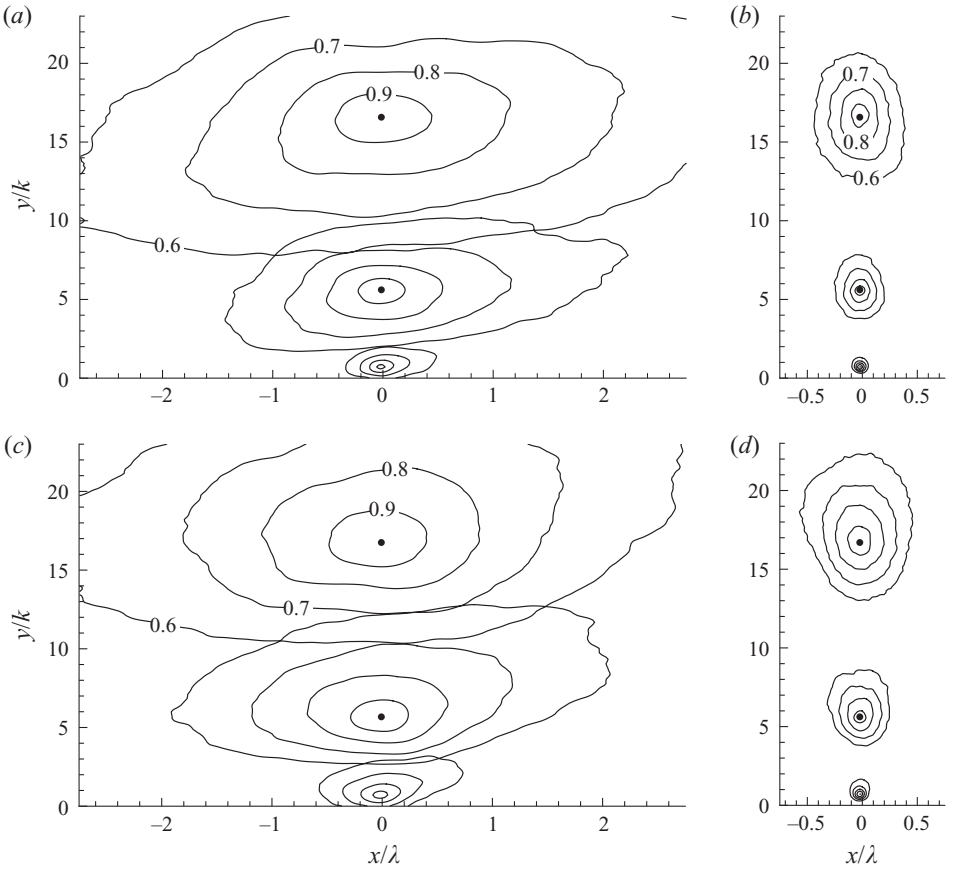

FIGURE 21. Quadrant-sampled two-point correlations: (*a*) $R_{uu,Q2}$, (*b*) $R_{vv,Q2}$, (*c*) $R_{uu,Q4}$, (*d*) $R_{vv,Q4}$ at $y = 0.6k$, $5.6k$ and $16.7k$ (shown by solid dots) for x–y plane 1 and $Re_\tau = 3520$.

ejections, especially below $y = 4k$–$5k$, because sweeps presumably bring down larger scale events from above, whereas ejections lift up small-scale eddies from below.

4. Discussion and conclusions

Utilizing an optically index-matched flow facility and high magnification PIV measurements, we have studied the turbulence statistics and flow structures in the inner part of a turbulent channel flow over a rough surface at Re_τ ranging from 3520 to 5360. In all cases, the combinations of Reynolds number, roughness and channel scales satisfy the well-characterized condition (Jiménez 2004). We focus mostly on the roughness sublayer and lower portions of the outer layer, but lower resolution data cover the entire half-channel. In the ensemble and spatially averaged turbulence statistics, $\overline{\langle u'u' \rangle}$ has a local maximum at $y = 4k \sim 5k$, while $-\overline{\langle u'v' \rangle}$ and $\overline{\langle v'v' \rangle}$ have relatively broad maxima at $y = 2k \sim 6k$ and $3k \sim 8k$, respectively. These trends are consistent with prior publications (Jiménez 2004). However, within the roughness sublayer, $\overline{\langle u'u' \rangle}$ increases again below $y = k$ as the wall is approached, peaking at the top of pyramidal elements. A slight increase also appears in the profile of $\overline{\langle v'v' \rangle}$ adjacent to the roughness while $-\overline{\langle u'v' \rangle}$ keeps on decreasing. Since small-scale structures are major contributors to the near-wall turbulence, the data are sensitive to the measurement resolution, especially when the wall-normal component

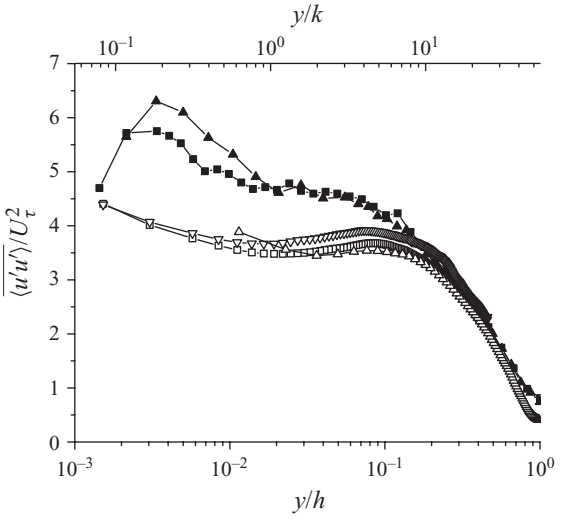

FIGURE 22. A comparison between the present $\overline{\langle u'u' \rangle}$ and the smooth-wall, channel flow data in Monty (2005). Present results: □, high-resolution data at $Re_h = 62\,500$; △, low-resolution data at $Re_h = 61\,600$; ▽, high-resolution data at $Re_h = 73640$. Monty's data: ■, $Re_h = 54\,000$; ▲, $Re_h = 70\,000$.

is involved. Even in our limited range of the Reynolds number, scaling of Reynolds stress components with U_τ^2 yields good collapse only far from the wall. In the $\overline{\langle u'u' \rangle}$ and $-\overline{\langle u'v' \rangle}$ profiles, maximum deviations occur in the vicinity of stress peaks in the $2k < y < 10k$ range, while the profiles of $\overline{\langle v'v' \rangle}$ continue to diverge as the wall is approached.

For the present roughness geometry, all the spatial variations in the mean velocity and Reynolds stress distributions vanish above $y \approx 2k$. To determine implications associated with the wall similarity hypothesis (Raupach *et al.* 1991), figure 22 compares the present, spatially averaged distribution of $\langle u'u' \rangle$ with the smooth-wall channel flow data available in Monty (2005) and Monty *et al.* (2009). To avoid issues related to Reynolds number effect, we only use smooth-wall data obtained at similar Reynolds numbers, i.e. $Re_h = 54\,000$ and 70 000. As is evident, the rough-wall results match those of Monty for $y/\delta > 0.1$–$0.2\,(y/k > 5$–$10)$, providing clear support for the Townsend's hypothesis for the Reynolds stress statistics. Slight deviations between profiles of $\langle u'u' \rangle$ and $\langle v'v' \rangle$ (not shown) can be attributed to uncertainties related to the curve fitting used for determining U_τ.

The effect of the roughness geometry becomes appreciable below $y \approx 2k$, where all distributions of the mean flow and turbulence statistics become highly variable but periodic with roughness wavelength. For example, the mean flow exhibits a channelling phenomenon, i.e. a higher streamwise velocity along slightly meandering paths located between the crests of pyramidal elements. Other phenomena associated with the flow separating and circumventing the pyramid crests are also evident. In the x–y plane dissecting the ridgeline, $\langle u'u' \rangle$ peaks above the forward-facing ridge of the pyramid, near the site of the maximal TKE production rate. While the contribution of shear to production is fairly uniform, spatial variations in the magnitude and sign of $\partial U/\partial x$ generate a TKE production peak above the forward ridge, in the region where the streamwise flow contracts. An inclined layer with high values of $\langle u'u' \rangle$ extends at a shallow angle away from the region of the maximum production. The distribution

of total wall-normal turbulent transport term also has a similar inclined pattern. The $-\langle u'v'\rangle$ peak coincides with that of $\langle u'u'\rangle$, while $\langle v'v'\rangle$ reaches local maximum slightly downstream. Within the roughness sublayer especially adjacent to the surface, a quadrant analysis shows that sweeps are the dominant contributors to the Reynolds shear stress and related statistical quantities such as shear production. During sweeps, the downward motions squeeze spatial non-uniformities into a thin layer within $y \approx 0.5k$ above the surface, leaving the flow above spatially uniform. Conversely, ejections expand the spatially non-uniform domain to the entire roughness sublayer. The contribution of ejections to all the Reynolds stress components exceeds that of sweeps above $y \approx 3k$ over the present range of Reynolds numbers. An analysis of terms in the TKE balance equation based on spatially averaged data shows that both production and dissipation rate (under-resolved) reach maximum at the elevation just above the top of pyramidal elements. However, $\bar{P}/\bar{\varepsilon}$ also peaks in the same region, causing substantial wall-normal turbulent transport near the wall. The latter becomes insignificant at higher elevations, leaving production and dissipation the only major contributors in the TKE balance. The magnitude of $\bar{P}/\bar{\varepsilon}$ drops to below one in the outer layer. These trends are consistent with the DNS results obtained by Ikeda & Durbin (2007) for the two-dimensional roughness.

The energy and shear spectra show an increasing contribution of large-scale motions, and a diminishing role of small-scale eddies with increasing distance from the wall. However, as the spectra steepen, $E_{11}(k_1)$, $E_{22}(k_1)$ and $E_{12}(k_1)$ develop bumps (flattening of slopes) in wavenumbers corresponding to k–$3k$. In the compensated energy spectra, these bumps appear as local maxima at scales corresponding to 15η–30η (which varies with elevation), i.e. within the dissipation range. A very similar trend can be seen in the oceanic data of Hackett *et al.* (2010), where the spectral bumps appear in wavenumbers corresponding to $\sim 1.6k$–$2.4k$ or 13η–20η, but in this case $k \sim 1$ cm and $\eta = 1.2$ mm. In both cases, these bumps appear at higher $k_1\eta$, i.e. deeper within the dissipation range, than those reported in Saddoughi & Verravalli (1994) for a smooth-wall boundary layer that have been attributed to an energy bottleneck. As demonstrated by sample instantaneous velocity and vorticity distributions, the roughness-scale eddies are generated near the surface, and advected rapidly away from the wall by large-scale structures that populate the outer layer. Consequently, in addition to eddies generated by the typical energy-cascading process of turbulence, the outer layer is also flooded by roughness-scale eddies that are produced near the wall, injecting excessive energy at these scales. Thus, although the imprints of roughness diminish in the outer-layer Reynolds stress statistics, in agreement with the wall similarity hypothesis, the small-scale turbulence and associated dissipation rate contain clear roughness signatures in the entire flow domain.

In an attempt to characterize the large-scale structures lifting near-wall eddies, we apply the swirling strength-based LSE along with observations on instantaneous data. Early signs of the formation of an inclined shear layer with ejection below and sweep above appear in the LSE results only above $y \approx 2.5k$. These features are similar to those observed by Christensen & Adrian (2001), and have been attributed to the formation of organized hairpin packets based on their analysis of experimental and numerical data (see comprehensive discussion in Adrian 2007). In the present data, the streamwise extent of the shear layer grows with elevation. However, such a shear layer does not appear closer to the wall in the LSE result, in spite of a substantial portion of instantaneous realizations showing that trains of roughness-scale eddies extend from the roughness at an inclined shallow angle. In the outer layer, where the LSE shear layer forms, it is still populated by roughness-scale eddies over the

entire flow domain. The presence of these eddies also obscures the shear layer entirely above $y \approx 8k$, but it reappears after lowpass filtering of the data. The outer layer LSE results also show the formation of multiple inclined structures with scales that are considerably larger than the roughness wavelength or distance from the wall. These scales are more related to the local turbulence integral scale, as observed in the spectral analysis. Such structures are also present in instantaneous realizations. Unfortunately, one cannot elucidate the three-dimensional profile and origin of these structures conclusively based on two-dimensional PIV data. Resolving them and their time evolution requires three-dimensional, time-resolved measurements that cover the region from the base of the pyramids. Ongoing holographic PIV measurements presently attempt to address this challenge.

This research has been funded by the Office of Naval Research under grant N00014-06-1-0650. The programme officer is Ronald Joslin. Construction of the optically index-matched facility has been funded by ONR, in part under grant N00014-06-1-0160, and in part by DURIP grant N00014-06-1-0556. The programme officer is Ki Han Kim. The authors would like to thank Yury Ronzhes for designing the new facility, as well as Siddharth Talapatra, Joshi Pranav and Huixuan Wu for their help during the experiments.

Appendix. Effect of spatial resolution on dissipation rate estimates

Dissipation estimates based on instantaneous velocity gradients are attenuated due to the finite spatial resolution of PIV measurements. In planar PIV, the in-plane spatial resolution is limited by the interrogation window size and the out-of-plane resolution is imposed by the laser sheet thickness or the depth-of-field (DOF) of the imaging system (Raffel *et al.* 2007), depending on which of the two is smaller. Meinhart, Wereley & Gray (2000) show that for a typical PIV analysis one should use the depth of correlation instead of DOF as the depth of the interrogation volume since out-of-focus particles still affect the intensity distribution of the image and, therefore, the velocity measurement. However, as described by Roth *et al.* (1999), we employ an enhancement procedure, which maintains the intensity distribution only above a locally determined threshold level, followed by histogram equalization. This process removes the background non-uniformities of images, including those of dim, out-of-focus particle traces below the threshold level. Consequently, DOF should be the proper length scale for the out-of-plane resolution of our data. The attenuation of velocity spatial gradients because of finite resolution is affected by the combination of the in-plane and out-of-plane resolutions. For the present high-resolution data, the interrogation window size is 126 μm, which is equal to 5η near the wall and $\sim 3\eta$ in the outer layer. The laser sheet thickness is about 0.5 mm $\sim 20\eta$. For high magnification images, where the particle image size is governed by the diffraction limit of the imaging system, the DOF can be estimated using (Inoué & Spring 1997)

$$\mathrm{DOF} = \frac{n\lambda_0}{NA^2} + \frac{ne}{NAM} \tag{A 1}$$

where NA is the numerical aperture, ~ 0.053 (using F# of ~ 9.5 of a Schneider Macro Componon-S 5.6/100 mm lens), λ_0 is the laser wavelength in vacuum, n is the refractive index, M is the magnification (1.86), and e is the pixel spacing of the CCD sensor. We use a diffraction limit-based formula since the characteristic size of particle traces on the CCD array is 2–3 pixels, corresponding to 8–12 μm, i.e. much larger

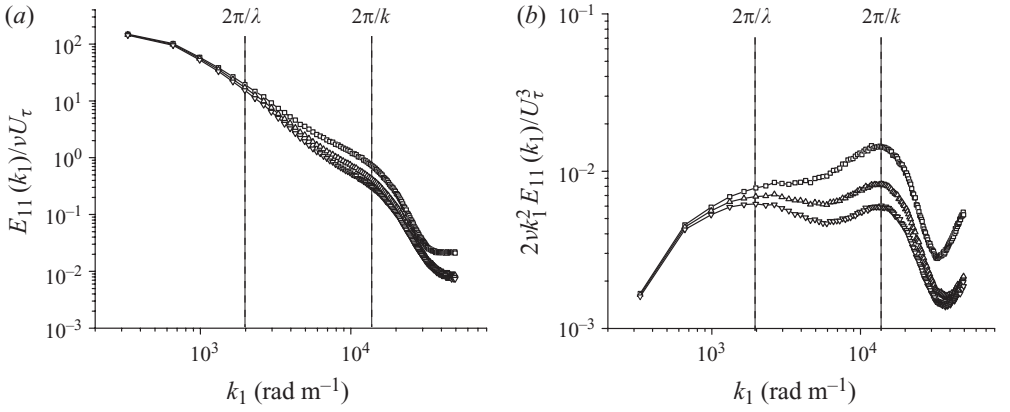

FIGURE 23. Attenuation caused by one-dimensional, wall-normal spatial averaging on (*a*) the streamwise energy spectrum, $E_{11}(k_1)/\nu U_\tau$, and (*b*) corresponding dissipation spectrum, $2\nu k_1^2 E_{11}(k_1)/U_\tau^3$ at $y/k = 3.4$. Symbols: □, original PIV data; △, filter size: DOF; ▽, filter size: laser sheet thickness.

than the actual particle size (2 μm). The resulting estimated DOF in our experiment is about 280 μm, i.e. 7η–13η. Because of the high magnification, the depth of focus is smaller than the laser sheet thickness.

On the basis of a study on the effect of the spatial resolution of PIV on dissipation estimates in decaying isotropic turbulence by Lavoie *et al.* (2007), the in-plane resolution should enable us to resolve about 75 % of the dissipation rate near the wall and 87 % in the outer layer. However, in their study the laser sheet thickness is chosen to be a half of the interrogation window size, while in our case, it is significantly larger than the in-plane values. Since we do not have a direct method for measuring the effect of the out-of-plane resolution on the in-plane derivatives, we estimate it instead based on an equivalent effect, namely the effect of spatial filtering in the wall-normal direction on the streamwise derivatives. We filter the original velocity field with a one-dimensional spatial top-hat filter and calculate its effect on squared perpendicular derivatives that appear in the dissipation rate formula. For example, wall-normal one-dimensional filtering is used for estimating the attenuation of $\langle(\partial u'/\partial x)^2\rangle$, and streamwise filtering for $\langle(\partial v'/\partial y)^2\rangle$. The analysis shows that for a filter with the size of the laser sheet thickness, $\langle(\partial u'/\partial x)^2\rangle$ and $\langle(\partial v'/\partial y)^2\rangle$ are attenuated by 64 % (62–67 %, depending on elevation) and 57 % (55–60 %), respectively. When DOF is selected as the filter size, the corresponding values are reduced to 56 % (53–59 %) and 45 % (42–48 %). Thus, a reasonable estimate for the attenuation of the dissipation estimates by the finite thickness of the laser sheet or depth of focus is about 50 %. Figures 23(*a*) and 23(*b*) show the effect of the one-dimensional, wall-normal, spatial filtering on sample streamwise energy spectra, $E_{11}(k_1)$, and dissipation spectra, $2\nu k_1^2 E_{11}(k_1)$. As expected, and consistent with the above discussion, the filtering causes significant attenuation, especially at high wavenumbers. However, the spectral bumps associated with roughness-scale eddies are evident before and after the filtering.

REFERENCES

ADRIAN, R. J. 2007 Hairpin vortex organization in wall turbulence. *Phys. Fluids* **19**, 041301.

ADRIAN, R. J., MEINHART, C. D. & TOMKINS, C. D. 2000 Vortex organization in the outer region of the turbulent boundary layer. *J. Fluid Mech.* **422**, 1–54.

Adrian, R. J. & Moin, P. 1988 Stochastic estimation of organized turbulent structure: homogeneous shear flow. *J. Fluid Mech.* **190**, 531–559.

Antonia, R. A., Kim, J. & Browne, L. W. B. 1991 Some characteristics of small-scale turbulence in a turbulent duct flow. *J. Fluid Mech.* **233,** 369–388.

Antonia, R. A. & Luxton, R. E. 1971 The response of a turbulent boundary layer to a step change in surface roughness. Part 1. Smooth to rough. *J. Fluid Mech.* **48**, 721–761.

Ashrafian, A., Andersson, H. I. & Manhart, M. 2004 DNS of turbulent flow in a rod-roughened channel. *Intl J. Heat Fluid Flow* **25**, 373–383.

Bakken, O. M., Krogstad, P.-Å., Ashrafian, A. & Andersson, H. I. 2005 Reynolds number effects in the outer layer of the turbulent flow in a channel with rough walls. *Phys. Fluids* **17**, 065101.

Bhaganagar, K., Kim, J. & Coleman, G. 2004 Effect of roughness on wall-bounded turbulence. *Flow Turbulence Combust*. **72**, 463–492.

Bigillon, F., Niño, Y. & Garcia, M. H. 2006 Measurements of turbulence characteristics in an open-channel flow over a transitionally-rough bed using particle-image velocimetry. *Exp. Fluids* **41**, 857–867.

Burattini, P., Leonardi, S., Orlandi, P. & Antonia, R. A. 2008 Comparison between experiments and direct numerical simulations in a channel flow with roughness on one wall. *J. Fluid Mech.* **600**, 403–426.

Champagne, F. H., Friehe, C. A., Larue, J. C. & Wyngaard, J. C. 1977 Flux measurements, flux estimation techniques, and fine-scale turbulence measurements in the unstable surface layer over land. *J. Atmos. Sci.* **34**, 515–530.

Christensen, K. T. 2004 The influence of peak-locking errors on turbulence statistics computed from PIV ensembles. *Exp. Fluids* **36**, 484–497.

Christensen, K. T. & Adrian, R. J. 2001 Statistical evidence of hairpin vortex packets in wall turbulence. *J. Fluid Mech.* **431**, 433–443.

Dancey, C. L., Balakrishnan, M., Diplas, P. & Papanicolaou, A. N. 2000 The spatial inhomogeneity of turbulence above a fully rough, packed bed in open channel flow. *Exp. Fluids* **29**, 402–410.

Dean, R. B. 1978 Reynolds number dependence of skin friction and other bulk flow variables in two-dimensional rectangular duct flow. *Trans. ASME: J. Fluids Engng* **100**, 215–223.

Djenidi, L., Antonia, R. A., Amielh, M. & Anselmet, F. 2008 A turbulent boundary layer over a two-dimensional rough wall. *Exp. Fluids* **44**, 37–47.

Falkovich, G. 1994 Bottleneck phenomenon in developed turbulence. *Phys. Fluids* **6**, 1411–1414.

Finnigan, J. J. 2000 Turbulence in plant canopies. *Annu. Rev. Fluid Mech.* **32**, 519–571.

Flack, K. A., Schultz, M. P. & Shapiro, T. A. 2005 Experimental support for Townsend's Reynolds number similarity hypothesis on rough walls. *Phys. Fluids* **17**, 035102.

Fujita, H., Yokosawa, H. & Hirota, M. 1989 Secondary flow to the second kind in rectangular ducts with one rough wall. *Exp. Therm. Fluid Sci.* **2**, 72–80.

Grass, A. J. 1971 Structural features of turbulent flow over smooth and rough boundaries. *J. Fluid Mech.* **50**, 233–255.

Hackett, E. E., Luznik, L., Katz, J. & Osborn, T. R. 2009 Effect of finite spatial resolution on the turbulent energy spectrum measured in the coastal ocean bottom boundary layer. *J. Atmos. Ocean. Technol.* **26**, 10–25.

Hackett, E. E., Luznik, L., Nayak, R. A., Katz, J. & Osborn, T. R. 2010 Field measurements of turbulence at an unstable interface between current and wave bottom boundary layer. *J. Geophys. Res.* (in press).

Hoyas, S. & Jiménez, J. 2008 Reynolds number effects on the Reynolds-stress budgets in turbulent channels. *Phys. Fluids* **20**, 101511.

Ikeda, T. & Durbin, P. A. 2007 Direct simulations of a rough-wall channel flow. *J. Fluid Mech.* **571**, 235–263.

Inoué, S. & Spring, K. 1997 *Video Microscopy: The Fundamentals.* Plenum.

Jiménez, J. 2004 Turbulent flows over rough walls. *Annu. Rev. Fluid Mech.* **36**, 173–196.

Keirsbulck, L., Labraga, L., Mazouz, A. & Tournier, C. 2002 Surface roughness effects on turbulent boundary layer structures. *Trans. ASME: J. Fluids Engng* **124**, 127.

Kim, J., Moin, P. & Moser, R. D. 1987 Turbulence statistics in fully developed channel flow at low Reynolds number. *J. Fluid Mech.* **177**, 133–166.

Krogstad, P.-Å., Andersson, H. I., Bakken, O. M. & Ashrafian, A. 2005 An experimental and numerical study of channel flows with rough walls. *J. Fluid Mech.* **530**, 327–352.

Krogstad, P.-Å. & Antonia, R. A. 1994 Structures of turbulent boundary layers on smooth and rough walls. *J. Fluid Mech.* **277**, 1–21.

Krogstad, P.-Å. & Antonia, R. A. 1999 Surface roughness effects in turbulent boundary layers. *Exp. Fluids* **27**, 450–460.

Krogstad, P.-Å., Antonia, R. A. & Browne, L. W. 1992 Comparison between rough and smooth-wall turbulent boundary layers. *J. Fluid Mech.* **245**, 599–617.

Lavoie, P., Avallone, G., De Gregorio, F., Romano, G. P. & Antonia, R. A. 2007 Spatial resolution of PIV for the measurement of turbulence. *Exp. Fluids* **43**, 39–51.

Lee, S. H. & Sung, H. J. 2007 Direct numerical simulation of turbulent boundary layer over a rod-roughened wall. *J. Fluid Mech.* **584,** 125–146.

Leutheusser, H. J. 1963 Turbulent flow in rectangular ducts. *J. Hydraulic Div. ASCE* **89**, HY3, 1–19.

Ligrani, P. M. & Moffat, R. J. 1986 Structure of transitionally rough and fully rough turbulent boundary layers. *J. Fluid Mech.* **162**, 69–98.

Lumley, J. L. 1967 Similarity and the turbulent energy spectrum. *Phys. Fluids* **10**, 855–858.

Luznik, L., Gurka, R., Nimmo Smith, W. A. M., Zhu, W., Katz, J. & Osborn, T. R. 2007 Distribution of energy spectra, Reynolds stresses, turbulence production, and dissipation in a tidally driven boundary layer. *J. Phys. Oceanogr.* **37**, 1527–1550.

Mathis, R., Hutchins, N. & Marusic, I. 2009 Large-scale amplitude modulation of the small-scale structures in turbulent boundary layers. *J. Fluid Mech.* **628**, 311–337.

Meinhart, C. D., Wereley, S. T. & Gray, M. H. B. 2000 Volume illumination for two-dimensional particle image velocimetry. *Meas. Sci. Technol.* **11**, 809–814.

Monty, J. P. 2005 Developments in smooth wall turbulent duct flows. PhD thesis, the University of Melbourne.

Monty, J. P., Hutchins, N., NG, H. C. H., Marusic, I. & Chong, M. S. 2009 A comparison of turbulent pipe, channel and boundary layer flows. *J. Fluid Mech.* **632**, 431–442.

Moser, R. D., Kim, J. & Mansour, N. N. 1999 Direct numerical simulation of turbulent channel flow up to $Re_\tau = 590$. *Phys. Fluids* **11**, 943–945.

Nimmo Smith, W. A. M., Katz, J. & Osborn, T. R. 2005 On the structure of turbulence in the bottom boundary layer of the coastal ocean. *J. Phys. Oceanogr.* **35**, 72–93.

Perry, A. E. & Li, J. D. 1990 Experimental support for the attached-eddy hypothesis in zero pressure-gradient turbulent boundary layers. *J. Fluid Mech.* **218**, 405–438.

Perry, A. E., Lim, K. L. & Henbest, S. M. 1987 An experimental study of the turbulence structure in smooth- and rough-wall boundary layers. *J. Fluid Mech.* **177**, 437–466.

Pope, S. B. 2000 *Turbulent Flows*. Cambridge University Press.

Raffel, M., Willert, C., Wereley, S. & Kompenhans, J. 2007 *Particle Image Velocimetry: A Practical Guide*, 2nd edn. Springer.

Raupach, M. R., Antonia, R. A. & Rajagopalan, S. 1991 Rough-wall turbulent boundary layers. *Appl. Mech. Rev.* **44**, 1–25.

Roth, G. I., Mascenik, D. T. & Katz, J. 1999 Measurements of the flow structure and turbulence within a ship bow wave. *Phys. Fluids* **11**, 3512–3523.

Saddoughi, S. G. & Veerravalli, S. V. 1994 Local isotropy in turbulent boundary layers at high Reynolds number. *J. Fluid Mech.* **268**, 333–372.

Schultz, M. P. & Flack, K. A. 2003 Turbulent boundary layers over surfaces smoothed by sanding. *Trans. ASME: J. Fluids Engng* **125**, 863–870.

Schultz, M. P. & Flack, K. A. 2007 The rough-wall turbulent boundary layer from the hydraulically smooth to the fully rough regime. *J. Fluid Mech.* **580**, 381–405.

Schultz, M. P. & Flack, K. A. 2009 Turbulent boundary layers on a systematically varied rough wall. *Phys. Fluids* **21**, 015104.

Seginer, I., Mulhearn, P. J., Bradley, E. F. & Finnigan, J. J. 1976 Turbulent flow in a model plant canopy. *Bound. Layer Meteorol.* **10**, 423–453.

Shah, M. K., Agelinchaab, M. & Tachie, M. F. 2008 Influence of PIV interrogation area on turbulent statistics up to 4th order moments in smooth and rough wall turbulent flows. *Exp. Therm. Fluid Sci.* **32**, 725–747.

Shockling, M. A., Allen, J. J. & Smits, A. J. 2006 Roughness effects in turbulent pipe flow. *J. Fluid Mech.* **564**, 267–285.

Soranna, F., Chow, Y. C., Uzol, O. & Katz, J. 2006 On the effect of IGV wake impingement on the flow around the leading edge of a rotor blade. *J. Turbomach.* **128**, 82–95.

Tachie, M. F., Bergstrom, D. J. & Balachandar, R. 2000 Rough wall turbulent boundary layers in shallow open channel flow. *Trans. ASME: J. Fluids Engng* **122**, 533–541.

Tachie, M. F., Bergstrom, D. J. & Balachandar, R. 2003 Roughness effects in low-Re_θ open-channel turbulent boundary layers. *Exp. Fluids* **35**, 338–346.

Townsend, A. A. 1976 *The Structure of Turbulent Shear Flow*, 2nd edn. Cambridge University Press.

Volino, R. J., Schultz, M. P. & Flack, K. A. 2009 Turbulence structure in a boundary layer with two-dimensional roughness. *J. Fluid Mech.* **635**, 75–101.

Wei, T. & Willmarth, W. W. 1989 Reynolds-number effects on the structure of a turbulent channel flow. *J. Fluid Mech.* **204**, 57–95.

Westerweel, J. 1997 Fundamentals of digital particle image velocimetry. *Meas. Sci. Technol.* **8**, 1379–1392.

Wu, Y. & Christensen, K. T. 2007 Outer-layer similarity in the presence of a practical rough-wall topography. *Phys. Fluids* **19**, 085108.

Yokoshawa, H., Fujita, H., Hirota, M. & Iwata, S. 1989 Measurement of turbulent flow in a square duct with roughened walls on two opposite sides. *Intl J. Heat Fluid Flow* **10**, 125–130.

Zhou, J., Adrian, R. J., Balachandar, S. & Kendall, T. M. 1999 Mechanisms for generating coherent packets of hairpin vortices in channel flow. *J. Fluid Mech.* **387**, 353–396.

Zhu, W., van Hout R. & Katz J. 2007 On the flow structure and turbulence during sweep and ejection events in a model canopy. *Bound. Layer Meteorol.* **124**, 205–233.

Zhu, Y. & Antonia, R. A. 1996 The spatial resolution of hot-wire arrays for the measurement of small-scale turbulence. *Meas. Sci. Technol.* **7**, 1349–1359.